This Book of Proceedings contains the extended abstracts of the contributions presented at the DIPSI Workshop 2025 on Droplet Impact Phenomena and Spray Investigation, organized by the University of Bergamo on Monday 13 June 2025 in Bergamo, Italy.

This workshop, which is now at its seventeenth edition, represents an important opportunity to share the recent knowledge on droplets and sprays in a variety of research fields and industrial applications.

The event is supported by the Department of Engineering and Applied Sciences of the University of Bergamo.

GIANPIETRO ELVIO COSSALI is full professor of Thermal Physics at the Department of Engineering and Applied Sciences of the University of Bergamo. His research activity is carried out in the field of thermo-fluid dynamics of multiphase systems, with particular reference to the characterization of sprays, to the dynamics of the interaction between droplets and solid and liquid surfaces and to the analytical modelling of heat and mass exchange in dispersed flows. He teaches the course of Thermal Physics, Thermo-fluid-dynamics and Heat transfer at the University of Bergamo.

SIMONA TONINI is Associate Professor of Thermal Physics at the Department of Engineering and Applied Sciences of the University of Bergamo. His research is carried out in the field of theoretical and numerical modelling of transport phenomena in multiphase flows. She teaches the course of Thermal Physics and the course of Thermal Physics for Advanced Technology for the Engineering degrees at the University of Bergamo.

ISBN: 978-88-97253-36-5
DOI: 10.13122/DIPSI2025

PROCEEDINGS OF THE DIPSI WORKSHOP 2024

PROCEEDINGS OF THE DIPSI WORKSHOP 2025

Droplet Impact Phenomena & Spray Investigations

BERGAMO, ITALY, 13rd JUNE 2025

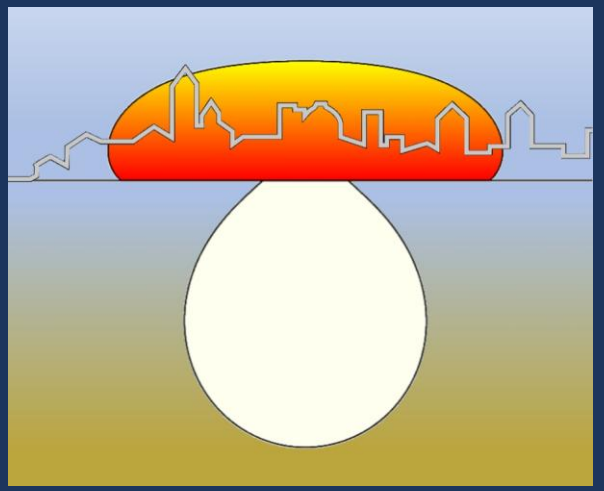

Edited by Gianpietro Elvio Cossali, Simona Tonini

UNIVERSITÀ DEGLI STUDI DI BERGAMO

2025

PROCEEDINGS OF THE DIPSI WORKSHOP 2025

Droplet Impact Phenomena & Spray Investigations

BERGAMO, ITALY, 13rd JUNE 2025

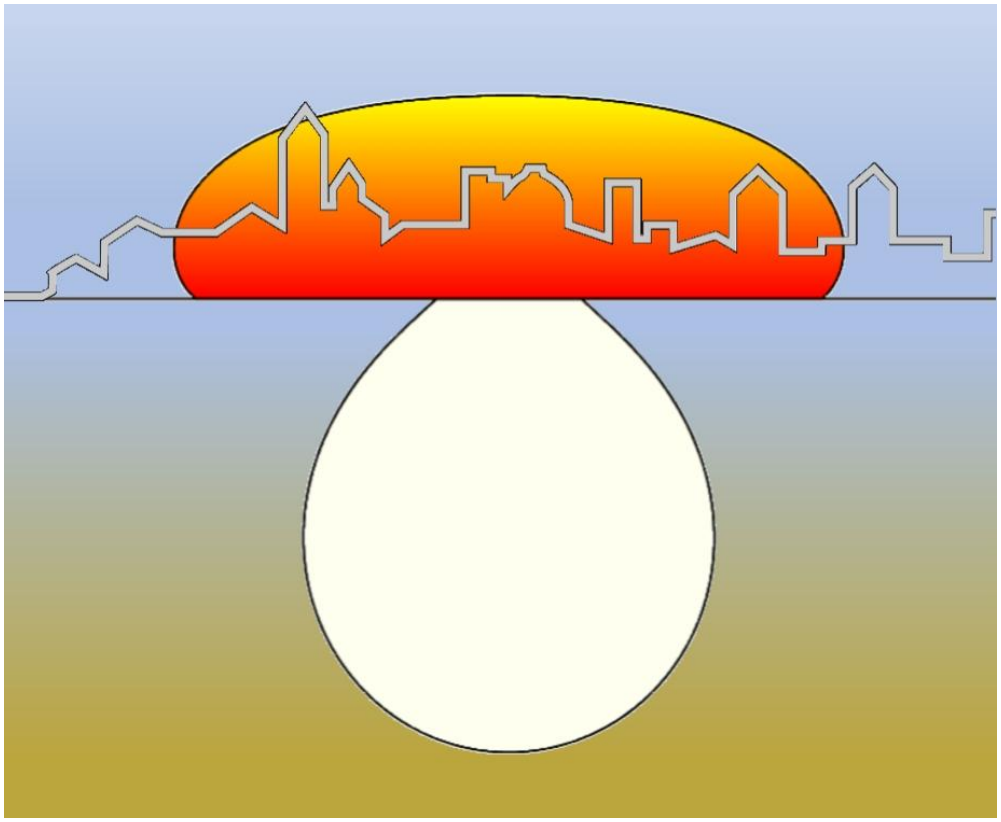

Edited by Gianpietro Elvio Cossali, Simona Tonini

Università degli Studi di Bergamo

2025

Proceedings of the DIPSI Workshop 2025: Droplet Impact Phenomena & Spray investigations, Bergamo, Italy, 13rd June 2025 / edited by Gianpietro Elvio Cossali, Simona Tonini – Bergamo: Università degli studi di Bergamo, 2025
ISBN: 978-88-97253-36-5
DOI: 10.13122/DIPSI2025

https://aisberg.unibg.it/handle/10446/328125

Progetto grafico: Servizi Editoriali
Università degli Studi di Bergamo
via Salvecchio, 19
24129 Bergamo
Cod. Fiscale 80004350163
P. IVA 01612800167

Workshop agenda, Monday 13 June 2025

08:45 Registration

09:00 Welcome speech

09:10 S1 Single drop experiment/modelling

9:10 S.S. Sazhin, A.V. Barsukov, D.V. Antonov, S.Y. Misyura, V.V. Terekhov, E.V. Shchepakina, V.A. Sobolev and P.A. Strizhak, *Modelling of heating and evaporation of multi-component liquid films: recent developments.*

9:40 P. Di Marco and A.I. Garivalis, *Measurement of interfacial stress from interface curvature*,

10:10 G. Lamanna, V. Mrotzek and C. Steinhausen, *Transcritical sprays: Towards drop sizing by polarized Mie scattering with structured illumination*

10:40 Coffee break

11:15 S2 Numerical methods

11:15 D. Ferrari, I. Peshkov, E. Romenski and M. Dumbser, *A structure preserving discretization of a unified HTC multiphase model of continuum mechanics.*

11:45 L.A. Botti and F.C. Massa, *A HHO formulation for variable density incompressible flows where the density is purely advected.*

12:15 Lunch break

13:30 Poster session

D.V. Antonov, O.V. Nagatkina, E.S. Sokolova, S.A. Kerimbekova, P.A. Strizhak and S.S. Sazhin S.S., *Aerosol flows in a human respiratory tract: experimental studies and modelling.*

L. Araneo, S. Musmeci and M. Marengo*, Impact of Sparkling Water Droplet: preliminary investigation.*

A. Lankry, Y. Amsalem, M. Vaknin, M. Arogeti and T. Bar-Kohany, *An Experimental Setup for Impingement of Liquid Gallium.*

D. Regener Roig, A. Colombo and A. Crivellini, *Towards discontinuous Galerkin solution of multiphase flows.*

R. Saha, C. Inal and B. Weigand, *DNS of ethanol droplet impact onto a smooth surface.*

S. Tonini, P. Conti and G.E. Cossali, Effect of natural convection on the modelling of *sessile and suspended evaporating drops.*

J. Wurst and K. Schulte, *Towards Direct Numerical Simulation of ternary systems in contact with a wall using PLIC-based contact line modelling.*

14:00 S3 Spray Investigations I

14:00 O. Magen, Y. Kozak, L. Di Lucchio, M. Marengo and T. Bar-Kohany, *Onset of flash boiling under rapid depressurization conditions across positive and negative pressure ranges – A theoretical model*

14:30 A. Amoresano, M. Dedes and V. Nebbioso, *Development of a neural network for determining the behavior of two-phase fluids: the case of sprays and drops.*

15:00 S4 Spray Investigations II

14:50 C. Stafford, Z. Nissar, G. de Sercey, S. Begg and O. Rybdylova, *Recent advances in droplet modelling using the Full Lagrangian Approach.*

15:15 N. Banerjee, M. Marengo and C. Tropea, *Analytical Prediction of Transient Spray Cooling.*

16:00 Coffee break

16:30 Workshop closure

Bergamo, 13 June 2025

Contents

Aerosol flows in a human respiratory tract: experimental studies and modelling

D.V. Antonov[1], O.V. Nagatkina[2], E.S. Sokolova[2], S.A. Kerimbekova[1], P.A. Strizhak[1], S.S. Sazhin[*1,3],
[1]National Research Tomsk Polytechnic University, 30, Lenin Avenue, Tomsk, 634050, Russian Federation
[2]Sechenov University, Moscow 119991, Russian Federation
[3]Kutateladze Institute of Thermophysics, Siberian Branch of the Russian Academy of Sciences, 1 Lavrentiev Avenue, Novosibirsk 630090, Russian Federation
*Corresponding author: sergei.sazhin@icloud.com

Introduction

The delivery of a drug into the human respiratory tract is one of the important tasks of inhalation therapy. Despite considerable progress achieved in the development of various delivery devices, inhalation is still one of the most complex types of drug therapy. A wide range of factors affecting the delivery to certain areas of the respiratory tract include the patient's application of the inhalation technique, variability of pulmonary function, and properties of the respiratory tract [8, 10]. Also, the drug properties, characteristics of delivery devices and individual characteristics of the human tracheobronchial tree affect the deposition of drugs in the respiratory tract [9].

The deposition fraction of inhaled drugs ranges from 2 to 67% of the nominal dose for the intrathoracic lungs (without the upper airway) [5]. The selection of the most appropriate inhaler depends not only on the type of drug and its dosage, but also on specific physical parameters of the delivery vehicle, and on the patient's inspiratory manoeuvre [11]. In the previously used approaches to modelling the heat and mass transfer processes in drug aerosol flows for delivery to the respiratory tract either the hydroscopic growth of aerosols due to the high humidity of ambient air in the respiratory tract was the dominant process modelled [6] or evaporation/condensation processes in these flows were ignored altogether [18]. Several studies focused on the evaporation processes in the respiratory tract were not related to the problem of drug delivery there (e.g. [13]). At the same time, aerosol evaporation during the delivery of a drug into the respiratory tract can have important effects on aerosol deposition at low ambient air moisture (less than 90%). This condition can be observed during breathing in dry ambient air, dehydration, respiratory diseases (for example, bronchial asthma, chronic obstructive pulmonary disease (COPD), and SARS) [15, 16, 17], and hyperventilation following a known mechanism of exercise-induced bronchoconstriction [7, 2].

Thus, the analysis of evaporating aerosol drug delivery in respiratory tract is important for practical medical applications, although this process has not been investigated so far to the best of our knowledge. Our investigation is specifically focused on the analysis of this case.

Materials and Methods

In-house experimental data were obtained in the form of averaged distributions of aerosol droplets by radii at the exit from the lower respiratory tract, printed on the Elegoo Saturn 3 Ultra 3D printer using Anycubic High Clear Resin as print material. A general view of the model prepared following this procedure is shown in Figure 1.

In order to make the inner surface of the model of the respiratory tract as close as possible to its real-life tissues, which have hydrophilic properties [14], the model was immersed in TWEEN 80 solution before the experiment, following the approach described by Salmanipour et al. [12]. The medicine approximated by water was sprayed using a constant flow jet nebulizer (Omron CompAir NE-C20 Basic Nebulizer (Omron Healthcare Inc)). A typical image of this spray (Spiriva® Respimat®) at 0.07 ms after the start of spray injection is shown in Figure 2.

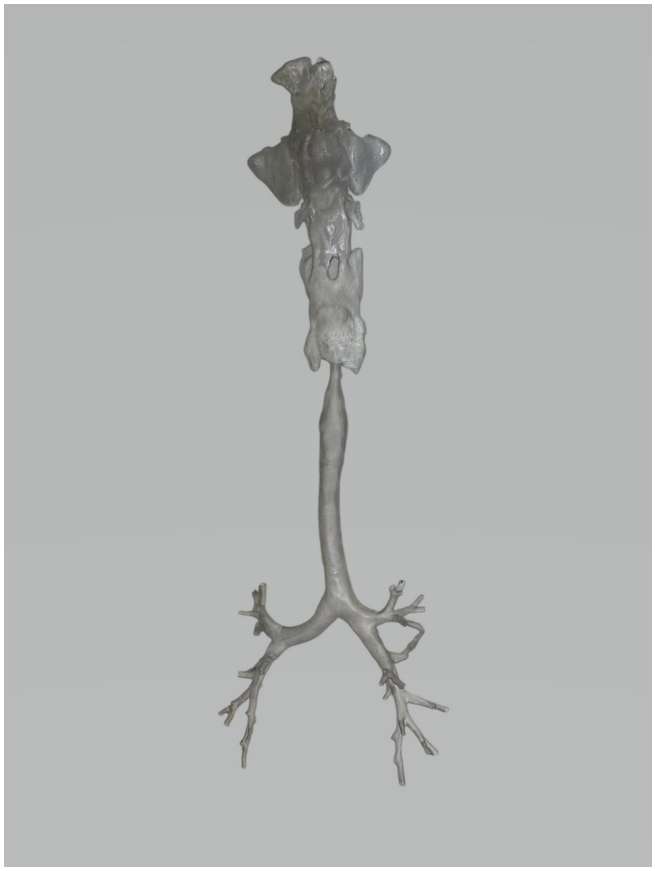

Figure 1. A general view of the respiratory tract used in the experiments.

The initial lognormal distribution of aerosols by sizes was assumed (the average aerosol radius was 4.0 ± 0.1 μm, their dispersion (geometric standard deviation (GSD)) was equal to 13.6 ± 0.1 μm, aerosol velocity was 0.22 ± 0.02 m/s. The flow of medical aerosols, generated by the nebulizer, was fed into the three-dimensional structure approximating the respiratory tract. Inhalation at a constant rate of 0.5 ± 0.1 m/s was simulated using a DSZH WK-115N vacuum pump. The initial temperature was the room temperature (300 ± 5 K).
Three-dimensional simulations, using COMSOL Multiphysics with the Heat Transfer, Fluid Flow, and Particle Tracing, were performed using the geometry shown in Figure 3. Model predictions were validated using experimental data presented in [1, 4] and in-house ones.

Results and Discussion

It was shown that the effects of aerosol heating and evaporation on their dynamics cannot be ignored when modelling the process of drug delivery in the human respiratory tract. This effect was shown to be particularly strong for patients with high body temperatures (higher than 310.15 K). It affected aerosol deposition in various regions of the respiratory tract taking into account the respiratory tract geometries for individual patients.
High human body (ambient) temperature is shown to increase the predicted rate of evaporation of aerosols leading to a decrease in their diameters. The latter was shown to affect the depth of penetration of aerosols into the respiratory tract and their deposition within it. When a certain threshold of this temperature (310.15 K) was reached, the aerosol deposition in the bronchi increased by 60% compared to the case when the process took place at normal human body temperature (309.75 K), assuming that aerosol velocity was 8 m/s, air flow velocity was 0.5 m/s, average aerosol diameter was 4.5 μm, and the number of aerosols was 10^5. It was demonstrated that most aerosols can deposit in the upper respiratory tract and least in the trachea. The asymmetry of bronchi location was shown to lead to asymmetry of deposition in the bronchi with deposition in the left bronchus up to about 80% higher than that in the right.

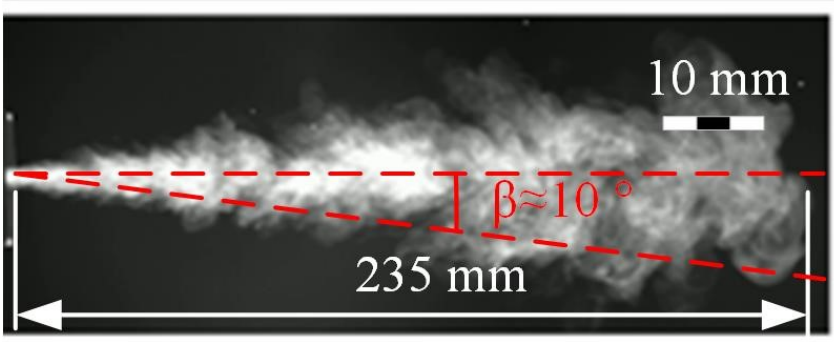

Figure 2. A typical image of medical aerosol spray (Spiriva® Respimat®) at 0.07 ms after spray injection.

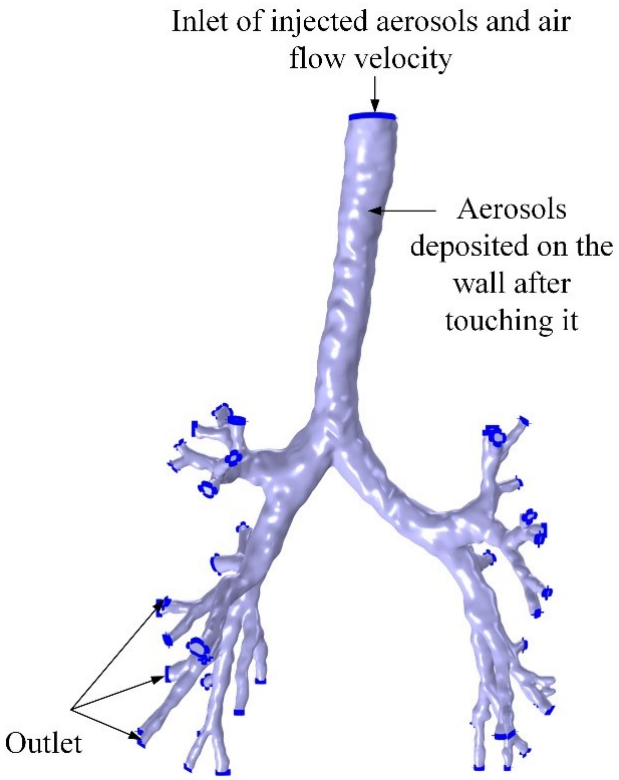

Figure 3. A geometry used in calculations of the flow, heat and mass transfer processes in drug aerosol streams for delivery to the respiratory tract. The image was prepared using the geometry provided by Bartol et al. [3].

The predicted deposition fractions of aerosols in three zones (trachea, left bronchus, and right bronchus) and for three ambient temperatures are compared in Figure 4. As can be seen in this figure, the deposition fractions strongly depend on both the temperature and the location (Zones 1, 2, and 3).

Conclusion

A thermophysical approach to controlling aerosol flows in a human airway was proposed to achieve maximum drug deposition, considering patients' individual characteristics (physiology of the airways and the architecture of the human tracheobronchial tree). The problem was addressed based on three-dimensional simulations using COMSOL Multiphysics with the Heat Transfer, Fluid Flow, and Particle Tracing modules. It was demonstrated that it is essential to take into account the processes of heat and mass transfer when simulating the flows of aerosols for targeted delivery to human airways at elevated temperatures (above 310.15 K). Using the database obtained from our study, conditions were formulated to increase the deposition rate of drugs in the respiratory tract. Hydrodynamic properties of aerosol fluxes were obtained

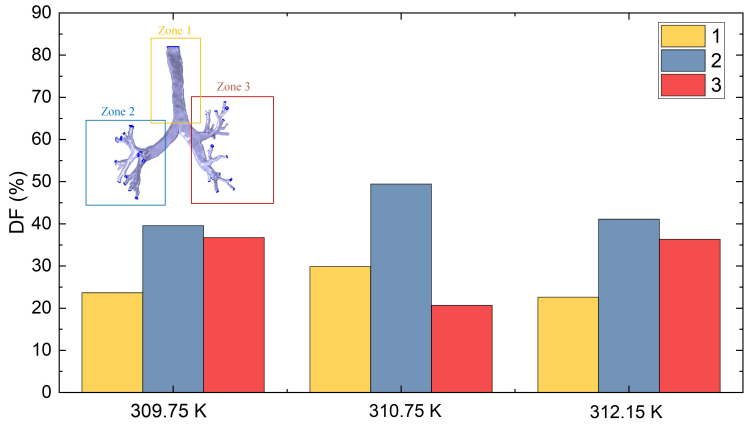

Figure 4. Aerosol deposition fractions (DF) in three respiratory tracts in the trachea (Zone 1), left bronchus (Zone 2) and right bronchus (Zone 3). Numbers in the figure show the number of the zone. Three temperature were used in calculations, as shown in the figure.

experimentally based on phase Doppler anemometry, shadow photography and tracer imaging. Three different inhalation drug delivery devices were used: Jet Nebulizer with Permanent Flow Metered Dose, Pressurized Aerosol Inhaler, and Soft Mist Type Inhaler (Respimat).

Acknowledgments

Research was supported by the Russian Science Foundation (project 24-45-00012, https://rscf.ru/project/24-45-00012/), and initiated during work on a project supported by the Royal Society (UK) (Grant no. IEC 192007).

References

[1] S. Ahmed and D. Giddens. *J. Biomech.*, 16:505–516, 1983.
[2] S. Anderson and P. Kippelen. *J. Allergy Clin. Immunol.*, 122:225–235, 2008.
[3] I. Bartol, M. Palomba, and M. Tano. *Commun. Eng.*, 3(1):152, 2024.
[4] Y. Cheng, Y. Zhou, and B. Chen. *Aerosol Sci. Technol.*, 31:286–300, 1999.
[5] A.-M. Ciciliani, P. Langguth, and H. Wachtel. *Int J Chron Obstruct Pulmon Dis.*, 12:1565–1577, 2017.
[6] D. Ciloglu. *J. Drug Deliv. Sci. Technol.*, 99:105978, 2024.
[7] D. Edwards and K. Chung. *QRB Discov.*, 4:e3, 2023.
[8] B. Florea, M. Cassara, H. Junginger, and G. Borchard. *J. Control. Release*, 87:131–138, 2003.
[9] X.-Y. He, M.-M. Han, Y.-C. Zhao, L. Tang, Y. Wang, L. Xing, N. Wei, J. Wang, G.-J. Wang, F. Zhou, J.-H. Jeong, and H.-L. Jiang. *J. Control. Release*, 376:972–984, 2003.
[10] S. Newman. *J. Aerosol Med.*, 8(s3), 1995.
[11] R. A. Pleasants and D. R. Hess. *Respir Care*, 63(6):i–831, 2018.
[12] S. Salmanipour, A. Sokhansanj, N. Jafari, H. Hamishehkar, and S. Saha. *Int. J. Pharm.*, 671:125171, 2025.
[13] C. Seyfert and A. M. J. Rodríguez-Rodrííguez, D. Lohse. *Phys. Rev. Fluids*, 7:023603, 2022.
[14] J. Sporty, L. Horálková, and C. Ehrhardt. *Expert Opin. Drug Metab. Toxicol.*, 4:333–345, 2008.
[15] R. Subramaniam, R. Richardson, K. Morgan, J. Kimbell, and R. Guilmete. *Inhal. Toxicol.*, 10:91–120, 1998.
[16] J. Wang, Y. Cai, X. Chen, B. Sun, and F. Tao. *Int. J. Heat Mass Transf.*, 219:124916, 2024.
[17] J. Xi and P. Longest. *Int. J. Heat Mass Transf.*, 51:5562–5577, 2008.
[18] Z. Zhang, C. Kleinstreuer, and C. Kim. *J. Aerosol Sci.*, 33:1635–1652, 2002.

Onset of Flash Boiling Under Rapid Depressurization Conditions Across Positive and Negative Pressure Ranges – A Theoretical Model

Omry Magen*[1], Yoram Kozak[1], Laura Di Lucchio[2], Marco Marengo[2], Tali Bar-Kohany[1,3]

[1]School of Mechanical Engineering, Tel Aviv University, Tel Aviv, Israel
[2]Department of Civil Engineering and Architecture, University of Pavia, Pavia, Italy
[3]Department of Mechanical Engineering, NRCN, Israel
*Corresponding author: omrymagen1@tauex.tau.ac.il

Introduction

Flash boiling atomization occurs when a liquid undergoes rapid depressurization below its saturation pressure, resulting in the formation of a fine spray characterized by wider spray angles and reduced penetration depth [1, 2]. This phenomenon is critical in various engineering applications, including fuel injection systems, cryogenic spray technologies, and carbon capture processes. Understanding the onset of nucleate boiling (ONB) [3] under rapid depressurization is essential for optimizing such systems, yet predicting nucleation conditions remains challenging due to the complex thermodynamic processes involved. [1]

The rate at which pressure decreases plays a crucial role in determining whether nucleation occurs through heterogeneous sites or if the liquid can penetrate deeper into the metastable region, potentially reaching spinodal conditions where spontaneous phase transition becomes inevitable [4].

This work presents an analytical thermodynamic model capable of predicting the ONB across both positive and negative pressure conditions. By leveraging classical nucleation theory (CNT) and introducing normalized thermodynamic parameters, the model establishes a universal correlation applicable to various fluids over a wide temperature range ($0.6 < T_r < 0.98$). The model addresses two fundamental questions: (1) What is the minimal depressurization rate required to reach spinodal conditions? (2) For a given depressurization rate and initial conditions, at what pressure does nucleation occur?

Theoretical Framework and Model Development

The classical nucleation theory provides a phenomenological approach to estimate nucleation rates by examining the energy barrier that must be overcome to form stable nuclei. For heterogeneous nucleation at solid-liquid interfaces, the nucleation flux is expressed as:

$$J = J_0 B \exp(-Gb\phi) \tag{1}$$

The Gibbs number, Gb, characterizes this barrier by comparing the minimal work required to form a critical nucleus with the thermal energy of the system:

$$Gb = \frac{W_{min}}{k_B T_c} = \frac{16\pi\sigma^3}{3k_B T(1 - v_l/v_v)^2 \Delta p_{ONB}^2} \tag{2}$$

where W_{min} is the critical work, k_B is Boltzmann's constant, T_c is the critical temperature, σ is surface tension, v_l and v_v are specific volumes of liquid and vapor phases. Δp_{ONB} represents the pressure difference between saturation and ONB [3] conditions. ϕ is the heterogeneity factor accounting for deviations from homogeneous conditions, and the pre-exponential factor is:

$$J_0 = \left(\frac{N_A}{v_l}\right)^{2/3}; \quad B = \frac{k_B T}{h_p} \tag{3}$$

with N_A being Avogadro's number and h_p Planck's constant.
At high degrees of superheating, curvature effects on surface tension become significant, which in turn, influences the nucleation flux predicted by the CNT [5]. The Tolman correction length is thus used to realize such dependency. Following [6], the following relationship is acquired:

$$\sigma(r,T) = \sigma_\infty - \delta\left(1 - \frac{v_l}{v_v}\right)\Delta p_{ONB} \tag{4}$$

where δ is the Tolman length, which varies with temperature according following [7] with fluid-specific constants which are determined through calibration with experimental data [6].
The Jakob number, representing the ratio of sensible to latent heat, can be reformulated using a linearized Clausius-Clapeyron relation:

$$Ja = \frac{\rho_l C_{p,l} T_{sat} \Delta p_{ONB}}{(\rho_v h_{fg})^2} \tag{5}$$

By normalizing the Jakob number relative to its maximum value at spinodal conditions, one obtains [6]:

$$Ja_r = \frac{Ja_{ONB}}{Ja_{sp}} = \frac{\Delta p_{ONB}}{\Delta p_{sp}} \tag{6}$$

This normalization reveals a fundamental relationship between the degree of superheating and the depressurization rate. It was shown in [8, 6] that by integrating J with respect to time while assuming a maximal bubble density on the solid wall surface (Z), the following simple expression can be acquired:

$$Z = \frac{J\Delta p_{ONB}}{\Sigma'} \tag{7}$$

where Σ' is the depressurization rate within the metastable region.
The relatively acquired depressurization rate ,$\Sigma'/\Sigma_{min,sp}$, is the experimental pressure drop rate normalized by the minimal required depressurization rate to reach the spinodal, $\Sigma_{min,sp}$. Inserting Eq. 7 into this definition reveals the proportion of superheating once again. Thus, the following statement can be formulated:

$$\frac{Ja}{Ja_{sp}} = F\left(\frac{\Sigma'}{\Sigma_{min,sp}}\right) \tag{8}$$

Results and Discussion
The model was validated against expansion tube experiments conducted on water, carbon dioxide, and R22 over an initial relative temperature range of $0.6 < T_r < 0.98$. Figure 1 presents the normalized Jakob number as a function of the normalized depressurization rate, demonstrating excellent collapse of data from different fluids and experimental conditions onto a single universal curve.
A semi-empirical correlation for the heterogeneity factor was developed based on the entire experimental database [6]:

$$\phi = 10^{(19.5T_r - 18.4)(1 - 0.4\Sigma_r^{0.8})} \tag{9}$$

This correlation successfully captures experimental results across the range $0.61 \leq T_r \leq 0.947$ and $10^{-9} \leq \Sigma_r \leq 0.99$ and is presented in Figure 2.
The successful collapse of experimental data from different fluids onto a single universal curve validates the theoretical framework and demonstrates the applicability of the normalized approach. The model's ability to predict nucleation across both positive and negative pressure regions represents a significant advance in understanding flash boiling dynamics.

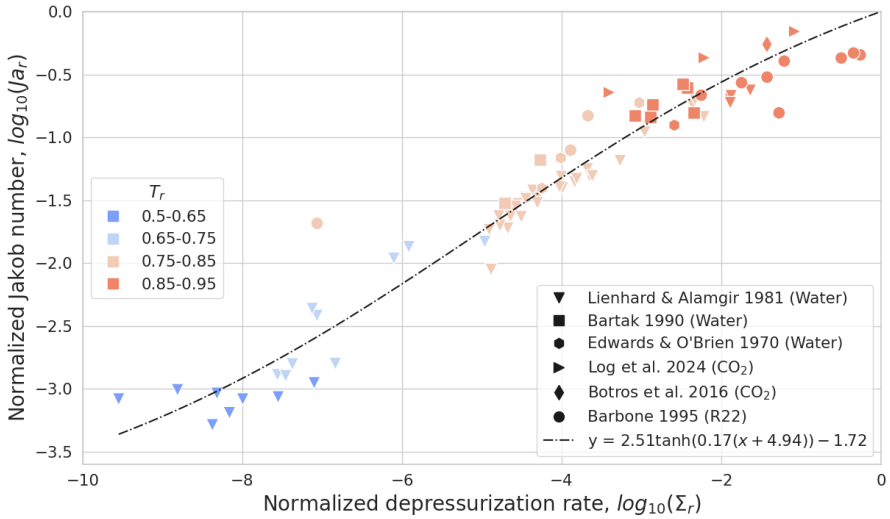

Figure 1. Normalized Jakob number vs. normalized depressurization rate showing universal behavior across different fluids: water (circles, stars, pentagons), CO_2 (crosses, plus signs), and R22 (triangles). The solid line represents the theoretical prediction. Adopted from Magen et al. [6]

The role of surface tension at high superheating levels is crucial for accurate predictions. Without accounting for curvature effects through the Tolman length correction, nucleation flux predictions would be orders of magnitude lower than physically realistic values, especially near the critical point.

The model provides practical tools for engineering applications in two ways: (1) as a standalone analytical method for quick predictions of ONB conditions, and (2) as a sub-model for implementation in computational fluid dynamics (CFD) simulations where the nucleation flux serves as a source term for bubble generation.

Conclusions

An analytical thermodynamic model has been developed to predict the onset of flash boiling under rapid depressurization conditions across positive and negative pressure ranges. The key findings include:

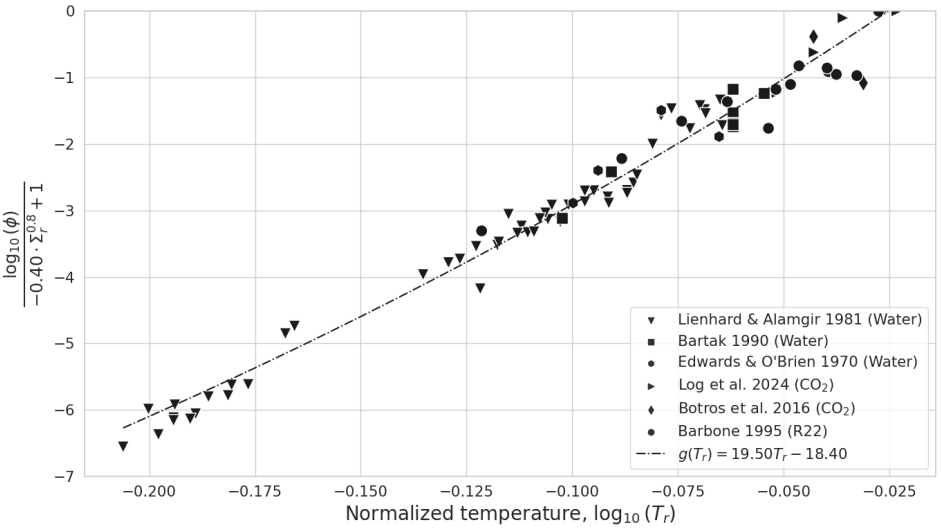

Figure 2. Heterogeneity factor function correlation using experimental data available: water (circles, stars, pentagons), CO_2 (crosses, plus signs), and R22 (triangles). The solid line represents the theoretical prediction. Adopted from Magen et al. [6]

The minimal depressurization rate required to reach spinodal conditions ($\Sigma_{min,sp}$) exhibits universal behavior across different fluids when properly normalized. The model successfully predicts nucleation pressures for given depressurization rates and initial conditions over a wide range ($0.4 < T_r \leq 0.98$, $10^{-9} \leq \Sigma_r \leq 1$). A new correlation for the heterogeneity factor extends applicability across diverse experimental conditions. The normalized Jakob number demonstrates a universal relationship with normalized depressurization rate, collapsing experimental data from water, CO_2, and R22 onto a single curve.Surface tension corrections accounting for curvature effects are essential for physically meaningful predictions at high superheating levels.

Nomenclature

B	Molecular collision frequency [s^{-1}]
C_p	Specific heat capacity [J/kg·K]
Gb	Gibbs number [-]
h_{fg}	Latent heat [J/kg]
h_P	Planck's constant [J·s]
J	Nucleation flux [$m^{-2}s^{-1}$]
Ja	Jakob number [-]
k_B	Boltzmann's constant [J/K]
N_A	Avogadro's number [mol^{-1}]
p	Pressure [Pa]
r	Radius [m]
T	Temperature [K]
v	Specific volume [m^3/kg]
W	Work [J]
Z	Nuclei density [m^{-2}]

Greek symbols

δ	Tolman length [m]
ϕ	Heterogeneity factor [-]
ρ	Density [kg/m^3]
Σ'	Depressurization rate [Pa/s]
σ	Surface tension [N/m]

Subscripts

c	Critical
l	Liquid
min	Minimal
ONB	Onset of Nucleate Boiling
r	Reduced/relative
sat	Saturation
sp	Spinodal
v	Vapor
∞	Low curvature reference

References

[1] E. Sher, T. Bar-Kohany, and A. Rashkovan, "Flash-boiling atomization," *Progress in energy and combustion science*, vol. 34, no. 4, pp. 417–439, 2008.

[2] T. Bar-Kohany, M. Arogeti, A. Malka, and E. Sher, "Advances in liquid atomization via flash boiling—a global overview," *Energies*, vol. 16, no. 19, p. 6763, 2023.

[3] T. Bar-Kohany, "Minimal heating rate for isobaric nucleation at the spinodal in liquids," *International Journal of Heat and Mass Transfer*, vol. 165, p. 120636, 2021.

[4] S. V.P, "Metastable liquids," 1974.

[5] M. E. M. Azouzi, C. Ramboz, J.-F. Lenain, and F. Caupin, "A coherent picture of water at extreme negative pressure," *Nature Physics*, vol. 9, no. 1, pp. 38–41, 2013.

[6] O. Magen, Y. Kozak, L. Di Lucchio, M. Marengo, and T. Bar-Kohany, "Predicting nucleation pressure under rapid depressurization: Bridging positive and negative pressure regions," *International Journal of Heat and Mass Transfer*, vol. 251, p. 127309, 2025.

[7] S. Gong, Z. Hu, L. Dong, and P. Cheng, "Temperature-and curvature-dependent surface tensions and tolman lengths for real fluids: a mesoscopic investigation," *Physics of Fluids*, vol. 35, no. 7, 2023.

[8] M. Alamgir and J. Lienhard, "Correlation of pressure undershoot during hot-water depressurization," *Journal of Heat Transfer*, vol. 103, no. 1, pp. 52–55, 1981.

Towards discontinuous Galerkin solution of multiphase flows

D. Regener Roig*[1], A. Crivellini[2], A. Colombo[1]
[1]Department of Engineering and Applied Sciences, University of Bergamo, Italy
[2] Department of Industrial Engineering and Mathematical Sciences, Polytechnic University of Marche, Italy
*Corresponding author: daniel.regener@unibg.it

Introduction

This project is devoted to the high-fidelity simulations of multiphase flows. Since the solutions of the multiphase models can present a wide range of scales, we constructed our solver using a modal discontinuous Galerkin (dG) method that is arbitrarily high-order and can seek for the solution in meshes composed of elements of any shape. In our path to the entropy-stable resolution of fully non-equilibrium models, we demonstrate the effectiveness of our proposed stabilization strategies and mass transfer formulation in a simpler model.

Modelling

We consider the multi-component compressible Euler model for two components and with a source term $\boldsymbol{b}$ [1], which is related to the mass transfer between phases

$$\frac{\partial \boldsymbol{q}}{\partial t}+\frac{\partial \boldsymbol{f}(\boldsymbol{q})}{\partial \boldsymbol{x}}=\boldsymbol{b}. \tag{1}$$

Where the conservative set and the physical flux are respectively

$$\boldsymbol{q} \coloneqq \left[\alpha_g\rho_g,\ \alpha_l\rho_l,\ \rho\boldsymbol{u},\ \rho e^t\right]^{\mathsf{T}}, \tag{2}$$

$$\boldsymbol{f} \coloneqq \left[\alpha_g\rho_g\boldsymbol{u},\alpha_l\rho_l\boldsymbol{u},\ \rho(\boldsymbol{u}\times\boldsymbol{u})+\boldsymbol{I}^{d\times d}p,\ (\rho e^t+p)\boldsymbol{u}\right]^{\mathsf{T}}, \tag{3}$$

and we close the model supplying it with the stiffened gas equation of state (EOS)

$$p_k(e_k,\rho_k)=(\gamma_k-1)\rho_k\left(e_k-e_{0,k}\right)-\gamma_k p_{\infty,k} \tag{4}$$

for each phase *k*. Finally, the equilibrium restrictions of the model are mechanical equilibrium ($p_l=p_g=p$) and thermal equilibrium ($T_l=T_g=T$).

Numerical solution

We consider a solution space $\mathbb{P}^{\kappa}$ constructed by a hierarchical and orthonormal basis in the mesh element T, [2] s.t

$$\mathbb{P}^{\kappa}=\{v_h\in L^2(\Omega)|v_{h|T}\in\mathbb{P}^{\kappa}(T),\forall T\in\mathcal{T}_h\}. \tag{5}$$

Hyperbolic part

We solve the hyperbolic part of the model using the modal dG method. By some manipulation, we obtain

$$\sum_{T\in\mathcal{T}_h}\frac{dQ_{k,j}}{dt}+\sum_{F\in\mathcal{F}_h}\int_F[\![\phi_j]\!]H_k\left(\boldsymbol{q}|_{K_+},\boldsymbol{q}|_{K_-},\boldsymbol{n}|_{K_+}\right)d\sigma+\sum_{T\in\mathcal{T}_h}\int_K\frac{\partial\phi_j}{\partial x_i}f_{k,i}(\boldsymbol{q})d\Omega=\boldsymbol{0}, \tag{6}$$

Where $Q_{k,j}$ are the components of the vector of unknown degrees of freedom. The previous system is integrated in time using a third-order strong stability preserving explicit Runge-Kutta (R-K) method under a CFL condition. We consider the Rusanov flux for H.

Instantaneous mass transfer

From the state obtained in the previous step, we apply a $p-T$ relaxation procedure [1] looking for a $\circ^*$ state defined by

$$\rho^*=\rho \qquad e^*=e \qquad \boldsymbol{u}^*=\boldsymbol{u} \qquad g_1^*=g_2^*. \tag{7}$$

regardless of the EOS used, this set of conditions lead to a system of equations

$$\begin{cases} g_l(p,T) - g_g(p,T) = 0 \\ \alpha_l(p,T)\rho_l(p,T)e_l(p,T) + \alpha_g(p,T)\rho_g(p,T)e_g(p,T) - \rho_0 e_0 = 0. \end{cases} \tag{8}$$

The conservation of total mass has been used to obtain the volume fractions as function of p and T as

$$\alpha_g(p,T) = \frac{\rho_0 - \rho_l(p,T)}{\rho_g(p,T) - \rho_l(p,T)} \tag{9}$$

The system is solved for p and T using a Newton-Raphson method. If one of the phases vanishes i.e. $\alpha_k \to 0$, we impose a negligible volume fraction $\alpha_{lim} = 10^{-8}$ and exit the mass transfer step.

Stabilization techniques

To ensure numerical robustness and physical consistency in the presence of strong gradients and complex flow regimes, we employ the following stabilization techniques.

Shock capturing

We apply the shock capturing term of [3] designed for ideal gases to the stiffened gases. The objective is to reduce instabilities at material interfaces, adding the following term to the discretization

$$\int_{\boldsymbol{K}} \varepsilon_w \left(\frac{\partial \boldsymbol{\phi}_h}{\partial x_i}\right)\left(\frac{\partial \boldsymbol{q}_h}{\partial x_i}\right) d\Omega, \tag{10}$$

where the shock sensor is

$$\varepsilon_w = C_{SC}\left(h_K^{SC}\right)^2 \sum_{n=1}^{3} \left(\frac{|S_n| + |D_n|}{\widetilde{\boldsymbol{w}_n^*}}\right) |\boldsymbol{d\tilde{q}}_j| \left(\frac{h_K^{SC}}{max(1,\kappa)}\right). \tag{11}$$

And is taken as the maximum value over the quadrature points on the element, and C_{SC} is a user-defined constant.

Positivity preserving strategy

We enforce the positivity of quantities that are physically defined to be non-negative by iteratively removing higher-order modes until positivity is achieved within the cell. The implementation of this procedure is computationally efficient due to the orthonormality of the basis functions

Results and Discussion

We now present two benchmark tests to evaluate the stability and accuracy of the proposed method. These cases involve strong discontinuities and phase change, making them well suited to demonstrate the effects of the chosen stabilization strategies.

Liquid-Vapour shock tube problem

It consists of a shock tube with a mixture of liquid water and water vapour. In Figure 1 it is shown that the presented shock capturing (qSC) applies dissipation at the contact interface, while a similar but pressure-based shock capturing (pSC) [4] does not. We denote the value of CSC following the name of the strategy used.

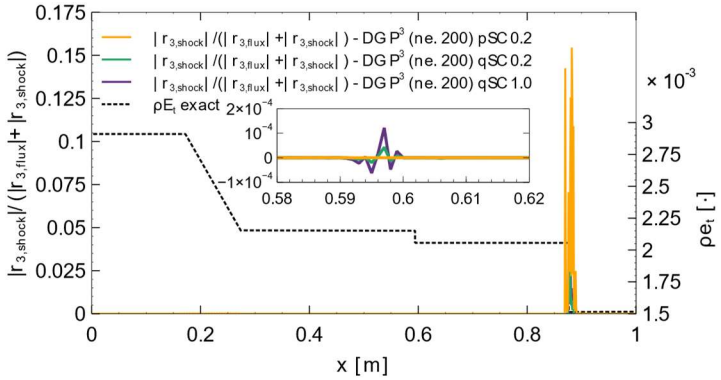

Figure 1. Results for the Liquid-Vapour shock tube problem with the same initial conditions as [1].

Depressurization of a CO_2 pipe

It is a shock tube problem where two distinct phases are present in the initial condition. Figure 2 presents the solutions both with and without mass transfer (MT). Reference numerical data from [1] has been extracted (digitized) directly from the original publication (---). When considering MT, the limiter is more active and affects at most the 4% of the elements per R-K stage.

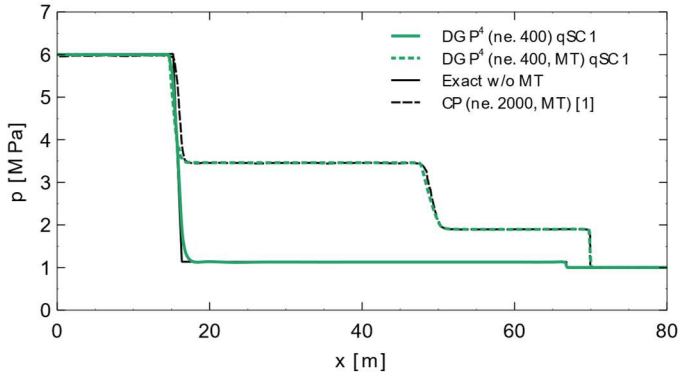

Figure 2. Results for the depressurization of a CO_2 pipe problem with the same initial conditions as [1].

Conclusion

The numerical method effectively handles mass transfer independently of the EOS and the results agree well with the literature. In our implementation, stabilization techniques were essential to prevent numerical failure during the simulation of 1D depressurization in a CO_2 pipe. While the results are encouraging, the positivity-preserving strategy remains intrusive and impacts the formal order of accuracy. Future developments will focus on extending the solver to multiple dimensions, eliminating the current equilibrium constraints, and reducing the impact of the positivity-preserving limiter.

Nomenclature

$\boldsymbol{q}$	Vector of conservative variables [various]	T	Element of the mesh [·]
$\boldsymbol{f}$	Physical flux vector [various]	$\mathcal{T}_h$	Set of elements of the mesh [·]
$\boldsymbol{b}$	Mass transfer source term [kg m^{-3} s^{-1}]	F	Face of the mesh [·]
$\boldsymbol{x}$	Space coordinates [m]	$\mathcal{F}_h$	Set of faces of the mesh [·]
α_k	Volume fraction of phase k [·]	Q	Solution vector [various]
ρ_k	Density of phase k [kg m^{-3}]	ϕ	Basis functions [·]
ρ	Mixture density [kg m^{-3}]	H	Numerical flux function [various]
$\boldsymbol{u}$	Mixture velocity [m s^{-1}]	K_+	External trace [·]
e^t	Total specific energy [J m^3 kg^{-1}]	K_-	Internal trace [·]
p_k	Pressure of phase k [Pa]	$\boldsymbol{n}$	Normal vector to F pointing outwards
e_k	Internal specific energy [J m^3 kg^{-1}]	ε_w	Shock sensor [·]
γ_k	Stiffened gas EOS constant [·]	h_K^{SC}	Element characteristic length [m]
$e_{0,k}$	Reference specific energy [J m^3 kg^{-1}]	S_n	Shock capturing term [various]
$p_{\infty,k}$	Stiffened gas EOS constant [Pa]	D_n	Shock capturing term [various]
T_k	Temperature of phase k [K]	$\boldsymbol{w}_n^*$	Corrected state vector for SC [various]
T	Mixture temperature [K]	$\boldsymbol{w}_n$	State vector vector for SC [various]
p	Mixture pressure [Pa]	$d\tilde{\boldsymbol{q}}_j$	Maximum normalized gradient of $\boldsymbol{w}_n$ [various]
κ	Polynomial degree of the solution space [·]	r	Residual of the spatial discretization [various]

References

[1] Bacigaluppi, P., Carlier, J., Pelanti, M., Congedo, P. M., Abgrall, R., Journal of Scientific Computing. 90: 1 (2022).
[2] Bassi, F., Botti, L., Colombo, A., Di Pietro, D.A., Tesini, P., Journal of Computational Physics 231: 45-65 (2012).
[3] Franchina, N., Savini, M., Bassi, F., Journal of Computational Physics 315: 302-322 (2016).
[4] Regener Roig, D., Crivellini, A., Colombo, A., Journal of Computational Physics 114808 (2026).

DNS of ethanol droplet impact onto a smooth surface

Rishav Saha*, Cemre Inal, Bernhard Weigand
Institute of Aerospace Thermodynamics, University of Stuttgart, Germany
*Corresponding author: rishav.saha@itlr.uni-stuttgart.de

Abstract

In this work, we studied the ethanol droplet spreading process and its dependence on the droplet Weber and Reynolds numbers. We investigated the spreading factor β [1], a critical parameter for characterizing droplet dynamics upon impact, for ethanol droplets over a Weber number range from 35 to 315, using Direct Numerical Simulation (DNS). Subsequently, the DNS results are validated against established empirical correlations. The spreading factor is then studied and compared for ethanol and water droplets. The study employs a Computational Fluid Dynamics (CFD) framework to simulate the impact process, solving the incompressible Navier-Stokes equations using the Finite-Volume method. The gas–liquid interface is defined using the Volume-of-Fluid (VOF) method [2], and the Piecewise Linear Interface Calculation (PLIC) method [3] is employed for interface reconstruction. The DNS tool Free Surface 3D [4] (FS3D), an in-house code at the Institute of Aerospace Thermodynamics, University of Stuttgart, is utilized.

Introduction

When a droplet impacts a surface with a high impact velocity, the droplet mostly splashes and forms secondary droplets, and some portion of the liquid sticks on the surface [1]. Whereas a droplet with a relatively lower impact velocity spreads on the surface without splashing. In this work, we investigated droplets with relatively lower impact velocity within the spreading regime. During this spreading process, the key dimensionless parameters [1] influencing the dynamics, the Weber number (We) and the Reynolds number (Re) are defined as follows:

$$We = (\rho D_0 U_0^2) / \sigma \quad , \qquad (1)$$

$$Re = (\rho D_0 U_0) / \mu \quad , \qquad (2)$$

where ρ is the liquid density, U_0 is the droplet impact velocity, D_0 is the initial droplet diameter, σ is the interface tension, and μ is the dynamic viscosity of the liquid. Figure 1 shows a schematic of a droplet impacting a smooth surface.

One of the most important dimensionless quantities for studying the impact process is the spreading factor [1]. The spreading factor β quantifies the extent to which a droplet spreads upon impact and is defined as the ratio of the maximum spreading diameter D_{max} to the initial droplet diameter D_0:

$$\beta = D_{max} / D_0 \quad . \qquad (3)$$

The spreading factor is influenced by both the Weber and Reynolds numbers. A higher value of the Weber and Reynolds numbers generally leads to an increased β. In many previous studies on the determination of the spreading factor β, various empirical formulas have been proposed for a range of Weber and Reynolds numbers, derived from experiments and analytical methods [5, 6, 7]. Table 1 summarizes the applicable ranges of Weber and Reynolds numbers for the empirical correlations from previous studies [5, 6, 7].

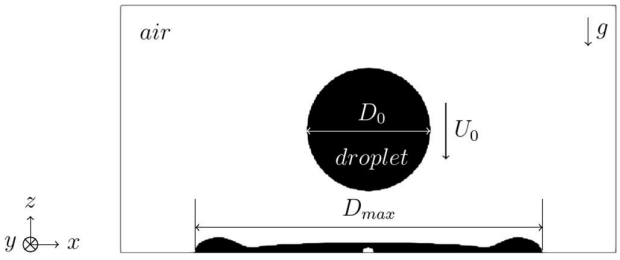

Figure 1. Schematic diagram of a droplet impacting onto a smooth surface. D_0 is the initial droplet diameter, impacting with a velocity of U_0, and D_{max} is the maximum spreading diameter. The liquid is shown in black.

Correlations		We valid range	Re valid range
$\beta = 1.27\ (Re^2\ Oh)^{0.122}$	Seo et al. [5]	12 < We < 1457	560 < Re < 6115
$\beta = 0.55\ (Re\ We^{0.5})^{0.18}$	Tian and Chen [6]	1.5 < We < 673	196 < Re <4104
$\beta = (Re^{0.2}\ We^{0.5}) / (7.6 + We^{0.5})$	Lee et al. [7]	1 < We < 1300	450 < Re < 18000

Table 1. Correlations are provided along with the corresponding ranges of Weber and Reynolds numbers for which the respective correlations of the spreading factor (β) are valid. The Ohnesorge number is defined as $Oh = We^{0.5} / Re$.

In this study, DNS were conducted for an ethanol droplet of D_0 = 1 mm impacting at different impact velocities onto a smooth surface, with a Weber number range of 35 to 315 (see Table 2) to study the spreading factor β. The flow is assumed to be incompressible and Newtonian, with no phase change. These results were validated using empirical correlations and compared with simulation results for water droplets. All simulations were performed for a flat surface with a static contact angle of 90°. Simulatons were run on the HPE Apollo Hawk supercomputer at the High-Performance Computing Center Stuttgart (HLRS), with a total simulation time of 3 ms for each case.

Results and Outlook

Table 2 presents the five simulated cases for ethanol droplets along with the corresponding DNS results. Figure 2 shows the validation of the DNS results for the spreading factor β, against empirical correlations [5,6,7]. A comparison of the spreading factors between ethanol and water droplet is also included in the same figure.

Case	I	II	III	IV	V
We	35	79	141	220	315
$Re^{0.2}$	3.66	3.97	4.2	4.39	4.56
β	2.45	2.85	3.18	3.45	3.69
$\tau_\beta = t\ (U_0 / D_0)$	1.55	2	2.35	2.75	3.05

Table 2. Summary of simulation parameters and corresponding results for ethanol droplet impact onto a smooth surface. The table lists the Weber number, Reynolds number to the power of 0.2, spreading factor β, and the dimensionless maximum spreading time τ_β for all five cases. Here, t is the physical time.

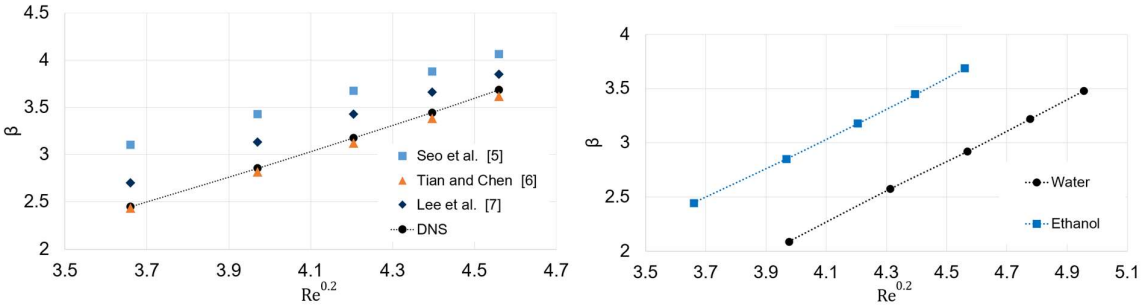

Figure 2. Left: Validation of the spreading factor (β) obtained from DNS for various Weber and Reynolds numbers, compared with different empirical models for ethanol droplets. Right: Comparison of the spreading factor predicted using DNS for ethanol and water droplet impacts.

It is observed that the spreading factor increases with rising Weber and Reynolds numbers within the viscous flow regime [1]. In addition, different liquid droplet experiences different spreading factor upon similar impact conditions. Therefore, to understanding the interplay between viscous, inertial and capillary forces during this dynamic process, different liquids must be studied. In future, FC-72 (refrigerant perfluorohexane) droplet impact onto a hydrophilic surface is simulated using dynamic contact angle models to predict β and dynamic spreading using DNS.

References

[1] C. Josserand and S. T. Thoroddsen. “Drop impact on a solid surface.” *Annual Review of Fluid Mechanics*, 48 (2016), pp. 365–391.

[2] C. W. Hirt and B. D. Nichols. “Volume of fluid (VOF) method for the dynamics of free boundaries.” J*ournal of Computational Physics*, 39(1) (1981), pp. 201–225.

[3] W. J. Rider and D. B. Kothe. “Reconstructing volume tracking.” *Journal of Computational Physics*, 141(2) (1998), pp. 112–152.

[4] K. Eisenschmidt, M. Ertl, H. Gomaa, C. Kieffer-Roth, C. Meister, P. Rauschenberger, M. Reitzle, K. Schlottke, and B. Weigand. “Direct numerical simulations for multiphase flows: An overview of the multiphase code FS3D.” *Applied Mathematics and Computation*, 272 (2016), pp. 508–517.

[5] J. Seo, J. S. Lee, H. Y. Kim, and S. S. Yoon. “Empirical model for the maximum spreading diameter of low-viscosity droplets on a dry wall.” *Experimental Thermal and Fluid Science*, 61 (2015), pp. 121–129.

[6] J. M. Tian and B. Chen. “Dynamic behavior of non-evaporative droplet impact on a solid surface: Comparative study of R113, water, ethanol and acetone.” *Experimental Thermal and Fluid Science*, 105 (2019), pp. 153–164.

[7] J. B. Lee, N. Laan, K. G. de Bruin, G. Skantzaris, N. Shahidzadeh, D. Derome, J. Carmeliet, and D. Bonn. “Universal rescaling of drop impact on smooth and rough surfaces.” *Journal of Fluid Mechanics*, 786 (2016), R4.

Modelling of heating and evaporation of multi-component liquid films: recent developments

S.S. Sazhin*[1], A.V. Barsukov[1], D.V. Antonov[1,2], S.Ya. Misyura[1], V.V. Terekhov[1], E.V. Shchepakina[3,1], V.A. Sobolev[3], P.A. Strizhak[1,2]

[1]Kutateladze Institute of Thermophysics, Siberian Branch of the Russian Academy of Sciences, 1 Lavrentiev Avenue, Novosibirsk 630090, Russian Federation
[2]National Research Tomsk Polytechnic University, 30, Lenin Avenue, Tomsk, 634050, Russian Federation
[3] Samara National Research University, Samara 443086, Russia
*Corresponding author: sergei.sazhin@icloud.com

Introduction

The modelling liquid film heating and evaporation and its various engineering applications have been widely discussed in the literature [6]. The application of the results of this modelling to spray cooling is perhaps the most widely known in engineering community. This cooling is widely used in metallurgy [8], electric vehicles to cool power batteries [1], electric motors [2], aerospace engineering [4], and electronics [3]. Particular attention has focused on spray cooling of high-power LEDs, where heat flux densities can reach 500 W/cm^2 (see Ref. [3]).
Although the practical importance of spray cooling is well known, many underlying physical processes that take place during its application are not well understood. Several studies indicate that the flow flux of the liquid is a key factor in determining the efficiency of heat removal during spray cooling [5, 9].
In this extended abstract, we will summarise recent results of the development on a simplified model that captures the key features of the processes in heated and evaporating liquid film and the validation of the results of this modelling. The main ideas of the model, described in this abstract, are based on the model of multi-component film heating/cooling and evaporation, described in [6, 7]. In that model, the analytical solutions to the one-dimensional heat transfer and component diffusion equations were used at each time step of the numerical code (analytical-numerical model). Some important limitations of the latter model, however, restricted its applicability with regard to many practically important engineering problems, including spray cooling. These were the assumption of a fixed wall temperature (Dirichlet boundary condition) and the absence of supply and removal of liquid from the film. These restrictions are removed in the new developments of the model briefly described below.

Materials and Methods

Model

The heat conduction equation inside the film, used in the analysis, is presented as:

$$\kappa_l \frac{\partial^2 T}{\partial x^2} = \frac{\partial T}{\partial t}, \tag{1}$$

where $\kappa_l = k_l/(c_l \rho_l)$ is the thermal diffusivity, k_l, c_l, and ρ_l are the thermal conductivity, the specific heat capacity, and the density of the liquid, respectively, x is the distance from the surface.
We assume that the temperature gradient at the surface is specified as:

$$\left.\frac{\partial T}{\partial x}\right|_{x=0} = Q_0, \tag{2}$$

where Q_0 is proportional to the heat flux supplied to the film from the surface (Neumann boundary condition).

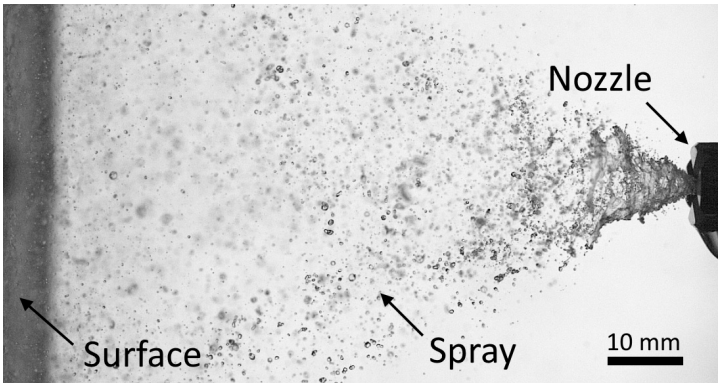

Figure 1. A photograph of a spray reaching the surface of the heat exchanger.

The boundary condition at the liquid film surface in the presence of a liquid supply to the film is formulated as the energy balance equation at this surface:

$$h(T_{\rm g} - T_{\rm s}) + \rho_{\rm l} L \dot{\delta}_{0e} + c_{\rm l}\rho_{\rm l}(T_{\rm spr} - T_{\rm s})\dot{\delta}_{\rm spr} = k_{\rm l} \left.\frac{\partial T}{\partial x}\right|_{x=\delta_0-0}, \tag{3}$$

where h is the convection heat transfer coefficient, $T_{\rm g}$ is ambient gas temperature, $T_{\rm s}$ is the surface temperature), $\rho_{\rm l}$ is liquid density, L is the specific heat of evaporation, $\dot{\delta}_e \leq 0$ is the rate of change of film thickness due to evaporation, $T_{\rm spr}$ is the sprays temperature, $c_{\rm l}$ is specific heat capacity of the liquid, $\dot{\delta}_{\rm spr} > 0$ is an increase in film thickness due to supply by spray, $k_{\rm l}$ is liquid thermal conductivity.

The analytical solutions to Equation (1) and the corresponding component diffusion equation in the liquids were used at each timestep of calculations. The predictions of the analytical solutions at the end of the timestep were used as initial conditions for the next timestep with adjusted values of input parameters.

The model predictions were validated using the results of in-house experimental data obtained using the setup described in the next section.

Experimental setup

Experimental investigations of heat transfer during the interaction of a spray with a heated surface were carried out on a specialised test bench equipped with a system supplying pressurised distilled water through a nozzle fitted with a solenoid valve. A stainless-steel heat exchanger measuring 70×70 mm with a thickness of 20 μm was positioned at a fixed distance from the nozzle and heated by a direct current power source, as shown in Figure 3.

Measurements of the temperature distribution on the surface were performed using infrared thermography on the reverse side of the heat exchanger (suface). Positions of the surface, liquid film and spray are shown in Figure 2.

The experiments included three series of studies: the first investigated pulsed surface cooling during short-term injection of a fixed liquid volume at a constant pressure drop under various thermal conditions; the second analysed the removal of heat from the surface during continuous supply of water to the film; the third focused on the removal of the liquid film from the surface after the cessation of liquid supply at a steady mass flow rate and specified heat fluxes. In all cases, the surface temperature dynamics was recorded.

Results and Discussion

Initially the surface was dry. The balance of heat supply from the heater and heat removal from the surface by convection led to the establishing of a fixed surface temperature equal about 61.7°C. The time evolution of the experimentally observed surface temperatures is shown in Figure 3 as red circles. Zone I in this figure refers to the last 10 s of the period of heating of the

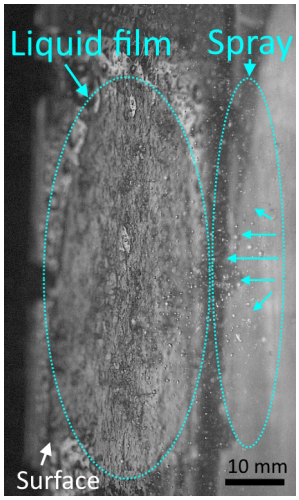

Figure 2. The same as Figure 3 but the photo was taken from a different direction and with a different focus.

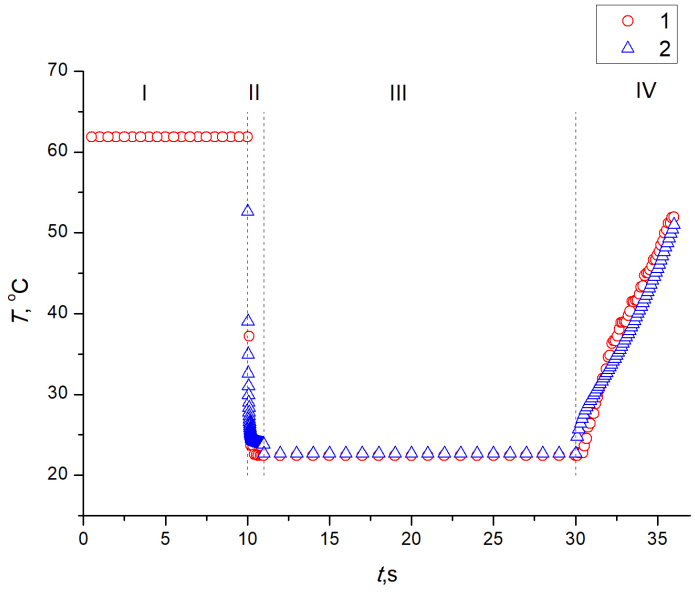

Figure 3. Observed (1) and predicted wall temperatures versus time.

dry surface.

At about 10 s spray is injected and water covers the whole surface. This leads to a rapid drop of surface temperature from around 61.7°C to around 22.4°C. This period of surface cooling is shown as zone II in Figure 3. At the next stage (zone III in Figure 3) continuous supply of water by spray and water removal from the liquid film lead to an establishment of almost constant film thickness and almost constant wall temperature of about 22.4°C. At the end of zone III, water supply to the film stopped but removal of water from the film continued. This led to a decrease in film thickness and an increase in wall temperature.

The results of temperature measurements during this process are shown in zone IV in Figure 3).

The results of modelling of these processes, using the approach described in the previous section, are shown in the same Figure 3. Good agreement between the experimental and modelling results are clearly seen in this figure.

Also, the model was generalised to consider the effect of possible formation of salt crystals in the salt solution. The predictions of this generalised model were shown to be reasonably close

to experimental observations.

Conclusion

The results of recent developments of the model of muti-component liquid film heating and evaporation are presented. These developments include considering the effect of continuous supply of liquid to the film, the effect of continuous supply of heat to the film via the surface, and the effect of possible formation of salt crystals in the salt solution. The new developments are based on a combined analytical and numerical approach when the analytical solutions to the heat transfer and component diffusion equations are implemented in the numerical code. The predictions of the new model are validated based on the in-house experimental results.

Acknowledgments

Research was supported by the Ministry of Science and Higher Education of the Russian Federation (Grant 075-15-2025-007) and initiated during work on a project supported by the Royal Society (UK) (Grant no. IEC 192007).

References

[1] I. Dhuchakallaya and P. Saechan. Enhancing the cooling efficiency of the air-cooling system for electric vehicle battery modules through liquid spray integration. *Journal of Energy Storage*, 72(E):108751, 2023.

[2] A. K. Kalajahi and P. S. Ghahfarokhi. High-viscosity spray cooling system for high-reliability motor drives in electric vehicles: a review. *IEEE Transactions on Transportation Electrification*, 11(1):3418–3432, 2025.

[3] S. Khandekar, G. Sahu, K. Muralidhar, E. Y. Gatapova, O. A. Kabov, R. Hu, X. Luo, and L. Zhao. Cooling of high-power leds by liquid sprays: Challenges and prospects. *Applied Thermal Engineering*, 184:115640, 2021.

[4] K. Li, Z. Liu, J. Xu, H. Liu, S. Xu, C. Wang, and J. Qin. Evaluation of high-speed aircraft thermal management system based on spray cooling technology: energy analysis, global cooling, and multi-objective optimization. *Applied Thermal Engineering*, 229:120632, 2023.

[5] I. Mudawar and W. Valentine. Determination of the local quench curve for spray-cooled metallic surfaces. *J. Heat Treat.*, 7:107–121, 1989.

[6] S. Sazhin, O. Rybdylova, and C. Crua. A mathematical model for heating and evaporation of a multi-component liquid film. *Int. J. Heat and Mass Transfer*, 117:252–260, 2018.

[7] S. S. Sazhin. *Droplets and Sprays: Simple Models of Complex Processes*. Elsevier, 2022.

[8] Q. Wang, J. Sun, J. Yang, H. Wang, L. Dong, Y. Jiao, J. Li, Z. Zhi, and L. Yang. Online partition-cooling system of hot-rolled electrical steel for thermal roll profile and its industrial application. *Special Issue Industrial IoT-Enabled Modeling and Optimization for the Process Industry*, 12(2):410, 2024.

[9] J. Yang, M. Pais, and L. Chow. Critical heat flux limits in secondary gas atomized liquid spray cooling. *Exp. Heat Transf.*, 6:55–67, 1993.

The effect of natural convection on the modeling of sessile and suspended evaporating drops

S. Tonini*, P. Conti and G.E. Cossali
Dept. Engineering and Applied Sciences, University of Bergamo, Italy
*Corresponding author: simona.tonini@unibg.it

Introduction

Motivation: Analytical models commonly assume that the mass transfer from a liquid drop in a stagnant environment is a diffusion-driven phenomenon. In the presence of external body forces, like gravitation, natural convection arises affecting the drop evaporation.
Objective: To study the effect of natural convection on the evaporation of sessile and pendant drops, considering the buoyancy caused by the variation in the gas density due to the uneven distribution of the vapour concentration and temperature in the gas mixture.

Materials and methods

The momentum, species and energy conservation equations are solved using ANSYS Fluent on 2D axis-symmetric grids, under steady-state conditions. The diffusive case is analytically modelled through the variable density model developed in [1, 2], applied to sessile and pendant droplets using the Picknett-Bexon correction [3] for spherical caps. Different values of the contact angle, drop size, drop and gas temperature and three different liquids were considered, see Table 1 for details.

Species	θ_c (°)	R_{eq} (mm)	T_d (°C)	T_{inf} (°C)	Gr (-)	Sc (-)	Mm (kg/kmol)
water	90	0.78-2.38	25	25	0.24-6.43	0.58	18
water	90	1.19	25-55	25-55	0.80-7.46	0.58-0.61	18
water	30-150	1.98	25	25	3.73	0.58	18
octane	90	0.634-1.59	20	20	0.49-7.59	2.28	114.23
octane	30-150	1.19	20	20	3.2	2.28	114.23
ethanol	90	0.634-1.59	25	25	0.50-7.76	1.15	46.07
ethanol	30-150	1.19	25	25	3.33	1.15	46.07

Table1. Test cases for the reported analysis

Model verification and validation

The model predictions were first validated by a comparison to the predictions of the analytical model reported in [1,2], by setting to zero the gravitational acceleration in the simulation so to exclude buoyancy, since the analytical model accounts only for vapour diffusion and Stefan flow while external convection is excluded. The results, shown in figure 1, right) are in very good agreement and the model, under these conditions, can be considered verified.

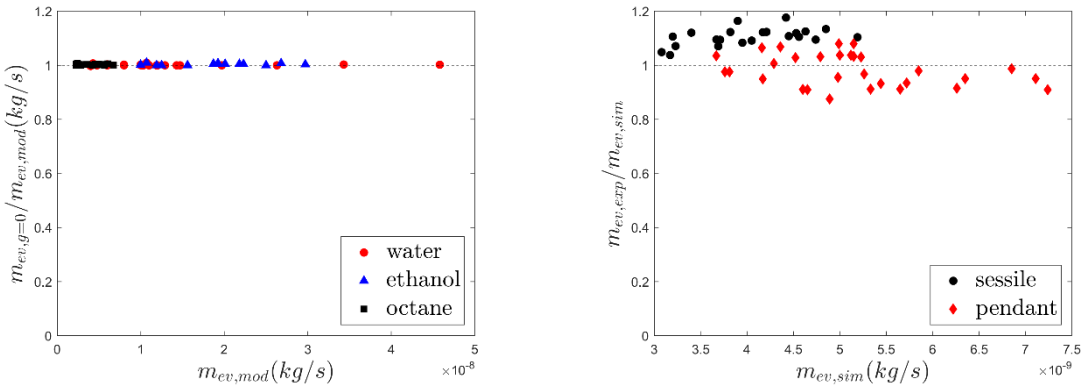

Figure 1. (Left) Comparison of the evaporation rate from the analytical model [1,2] predictions and from the numerical simulations with g=0; (right) validation of the CFD results against experiments [4].

A model validation was also performed by comparison to the results from the experimental work as reported in [4]. The comparison shows acceptable consistency, with some overestimation for the pendant drop case (see figure 1, right).

Results and Discussion

The flow field and vapour mass fraction around the evaporating drops are reported in figure 2 for four different cases. The buoyancy flow is directed as gravity in air/octane or air/ethanol gas mixture, supporting vapour convection with pendant drops (the flow is directed away from the wall, AW) and opposing it with sessile drops (the flow is directed towards the wall, TW). The contrary occurs with water drops. The effect is explained observing that water has a molar mass lower than that of air, then the gas flow is always directed in the direction opposite to the gravity acceleration, i.e. away from the wall for sessile drops and toward the wall for pendant drops. Octane and ethanol instead have molar mass larger than that of air and then the direction of the flow is the opposite: toward the wall for sessile drop and away from the wall for pendant drops.

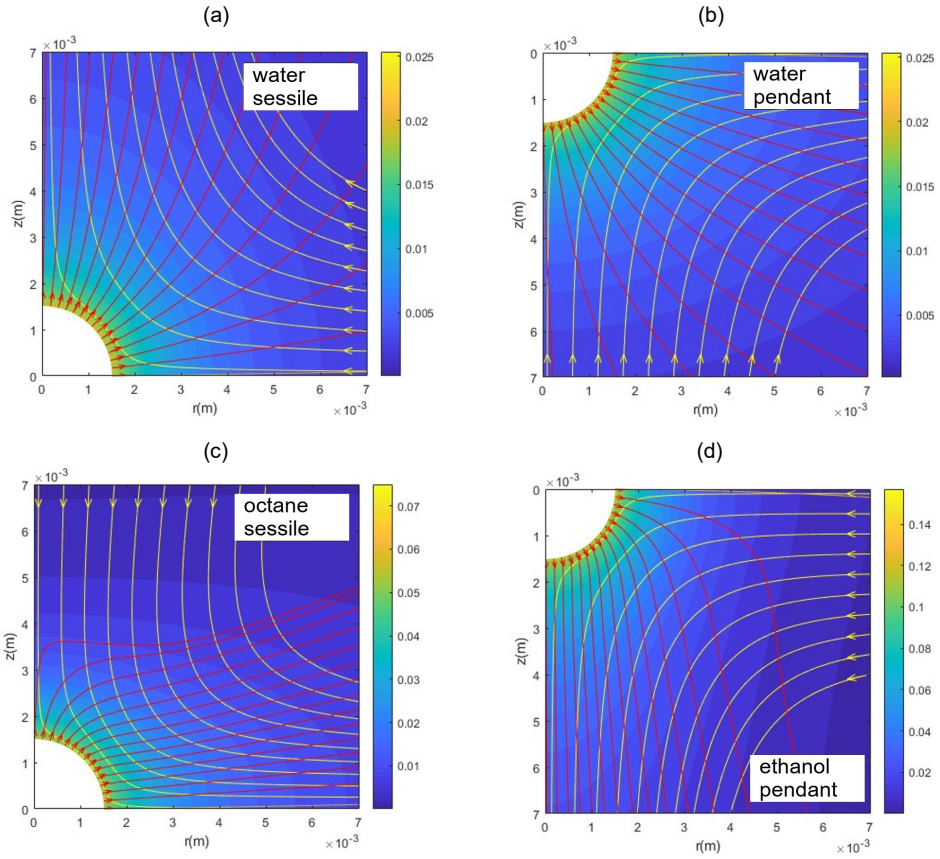

Figure 2. Distribution of the vapour mass fraction and streamlines of gaseous mixture (yellow lines) and vapour (red lines) for drops with Req= 1.19 mm and θ_c = 90° made of: (a) water-sessile (TW), (b) water-pendant (AW), (c) octane-sessile (TW), (d) ethanol-pendant (AW).

This different flow behaviour with respect of the molar masses of the evaporating species explain why that sessile water drops show higher evaporation compared to suspended ones and the opposite occurring for ethanol and octane drops, with differences increasing with the Grashoff number as shown in figure 3(left). The re-classification of the results in term of flow direction (toward or away from the wall) instead of pendant or sessile geometry eliminates the apparent inconsistency seen in figure 3(right). Figure 3(right) reports the results using this classification, showing the quantity $\Psi=m_{ev}/m^0_{ev}-1$ where m_{ev} is the evaporation rate in the presence of natural convection while m^0_{ev} is that in the absence of natural convection.

The substrate wettability has a small influence on the evaporation rate when the contact angle is comprised between 60 deg and 120 deg, while a non-negligible effect is observed for more hydrophilic and more hydrophobic substrates, up to about 24% and 29% with contact angles equal to 30° and 150°, respectively.

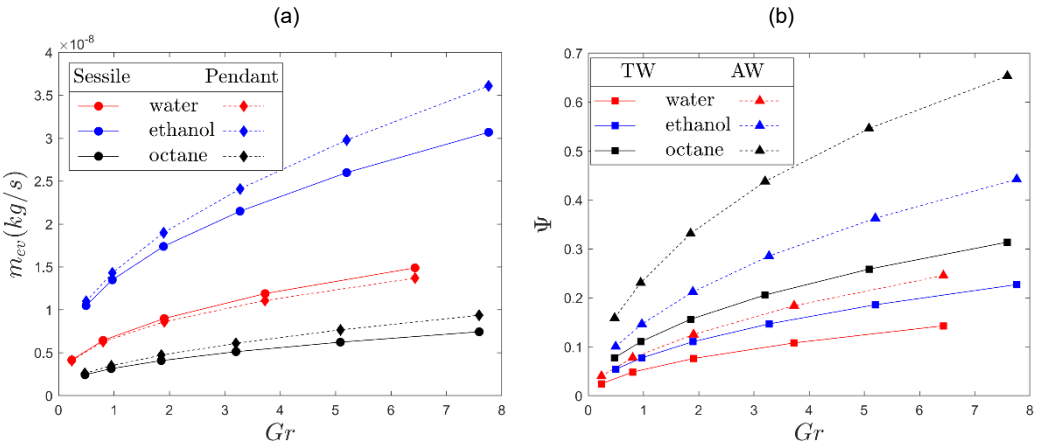

Figure 3. Effect of the Grashoff number on (left) the evaporation rate and on (right) relative difference of the evaporation rates with and without natural convection, predicted by the numerical model for pendant and sessile drops, and three liquids. θ_c = 90°.

In the attempt of correlating the results the quantity Ψ is written as a function of Grashoff and Schmidt numbers of the form:

$$\Psi = A\, Gr^m\, Sc^n \qquad (1)$$

Figure 4 shows the first results by comparing the values obtained from the simulation, Ψ_{num}, to those predicted by the correlation, Ψ_{num}. A better agreement is found by formulating two different correlations for the cases of flow directed toward the wall (TW) and away from the wall (AW).

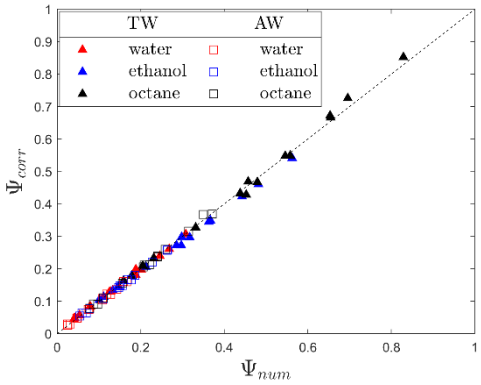

Figure 4. Comparison of the non-dimensional evaporation rate predicted by the numerical model and by the empirical correlation, for all the tested operating conditions.

Work-in-progress: effect of drop deformation

The drop deformation induced by gravity seems to have a non-negligible effect on the evaporation in presence of natural convection when the drop size increases.

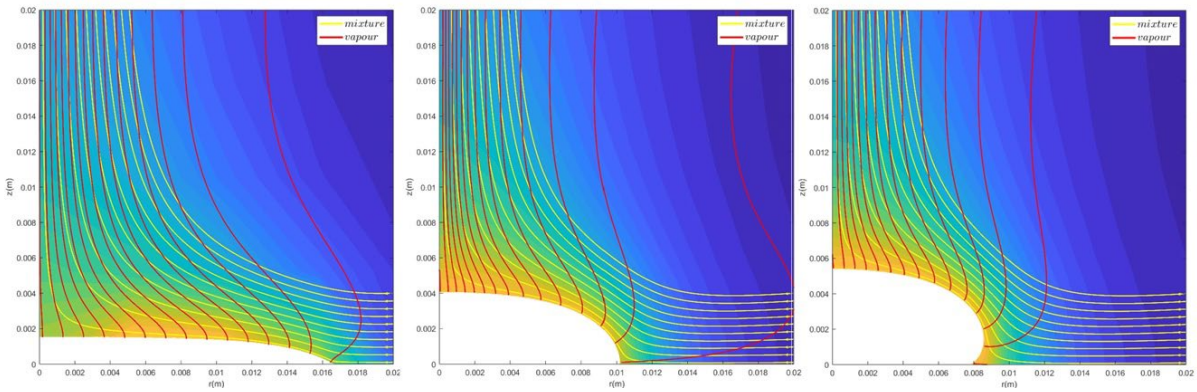

Figure 5. Distribution of the vapour mass fraction and streamlines of gaseous mixture (yellow lines) and vapour (red lines) for deformed water drops with R_{eq} = 6.102 mm (Bo = 5) and contact angle (a) θ_c = 30°, (b) θ_c = 90°, (c) θ_c = 150°.

Preliminary results obtained with water drops with Bond number about 5 (see figure 5 for the flow fields) suggest that the effect of natural convection on the evaporation rate, compared to the purely diffusive case, is about 133%, 94% and 89% for drops with contact angle equal to 30°, 90° and 150°, respectively.

Conclusions

The effect of natural convection on the evaporation of sessile and pendant drops was studied in a range of Grashoff number up to 7.76, Schmidt number up to 2.28, and contact angle between 30° and 150°.

The comparison between the results from the numerical simulations assuming g=0 and the analytical model shows an average difference of about 0.25%, while the discrepancies with the experiments are always lower than 20%. Buoyancy flow promotes the vapour convection with ethanol or octane pendant drops and the opposite with sessile drops. The contrary occurs with water drops.

The effect of wettability is lower than about 5% with contact angle between 60°- 120° respect to the case with 90°, up to 24-29% with contact angle of 30°.

The average discrepancy between the correlation and the numerical predictions is about 3.1% (about 3% for TW cases and 2.7% for AW).

References

[1] S. Tonini, G. Cossali, Int. J. Therm. Sci. 57, 45–53 (2012).
[2] S. Tonini, G. Cossali, E. Shchepakina, V. Sobolev, S. Sazhin, Phys. Fluids 34, 073312 (2022).
[3] R. Picknett, R. Bexon, J. Colloid and Interface Science 61, 336–350 (1977).
[4] S. Tonini, P. Conti, G. Cossali, E. Starinskaya, N. Miskiv, A. Rodionov, S. Starinskiy, V. Terekhov, and S. Sazhin, Phys. Fluids 37

Towards Direct Numerical Simulation of ternary systems in contact with a wall using PLIC-based contact line modeling

J. Wurst*[1], K. Schulte[1]
[1]Institute for Aerospace Thermodynamics, University of Stuttgart, Germany
*Corresponding author: jonathan.wurst@itlr.uni-stuttgart.de

Introduction

Drop wall interactions involving not only one liquid but another immiscible liquid phase offer great potential in advanced applications such as cell printing or oil remediation. Being able to simulate such processes helps in understanding and designing them. We therefore develop a simulation framework to simulate a ternary system in contact with a wall. Starting from the framework of Potyka and Schulte [4], our in-house multiphase flow solver *Free Surface 3D* [2] is extended to accurately simulate the associated contact line dynamics at the wall. The contact angle boundary condition proposed by Sussman [6] is extended for the second liquid phase and applies a local averaged contact angle to distinguish between the contact lines. A short introduction to the theory on compound sessile drops is then followed by several static tests of the code.

Material and methods

The in-house code *Free Surface 3D* (FS3D) [2] is further developed for a ternary system in contact with a wall. It is based on the Finite Volume method and applies the Volume-of-Fluid method (VoF) [3] together with the piecewise linear interface calculation (PLIC) [5] to distinguish between the phases. For the reconstruction of the interface, the method proposed by Potyka and Schulte [4] is employed. Where an interface is in contact with a solid boundary, the surface tension force has to be adjusted according to the wettability. This is usually achieved by imposing a specific contact angle. For this purpose, we extend the method of Sussman [6] to be able to simulate three immiscible phases in contact with a wall.

Contact Angle Boundary Condition - At a wall boundary, there is no full stencil available for the calculation of the surface tension force. The idea of Sussman's method [6] is to provide this missing information by extending the interface into the ghost cells. This approach is independent of the surface tension model and can be applied to immersed boundaries as well. With the wall normal $\mathbf{n}_{wall}$ and the interface normal $\mathbf{n}_f$, an artificial velocity $\mathbf{u}_{ext}$ is constructed by

$$\boldsymbol{u}_{ext} = \frac{\boldsymbol{n}_{wall} + \cot(\theta)\boldsymbol{n}_2}{|\boldsymbol{n}_{wall} + \cot(\theta)\boldsymbol{n}_2|}, \tag{1}$$

$$\boldsymbol{n}_2 = -\frac{\boldsymbol{n}_1 \times \boldsymbol{n}_{wall}}{|\boldsymbol{n}_1 \times \boldsymbol{n}_{wall}|}, \tag{2}$$

$$\boldsymbol{n}_1 = -\frac{\boldsymbol{n}_f \times \boldsymbol{n}_{wall}}{|\boldsymbol{n}_f \times \boldsymbol{n}_{wall}|}, \tag{3}$$

where $\mathbf{n}_1$ and $\mathbf{n}_2$ are auxiliary vectors in the wall plane and point tangential and orthogonal to the contact line, respectively. By executing several steps of the advection scheme with an artificial time step of $\Delta t = 0.5\Delta z|\boldsymbol{u}_{ext}|^{-1}$, the ghost cells are filled with liquid and provide information about the interface.

With a second immiscible liquid phase, two more types of contact lines can form with distinct contact angles θ_{ij} between the phases i and j. A sketch of such a situation is displayed in Figure 1. Throughout this paper, we specify the continuous gaseous phase as phase 3 and the liquid phases as 1 and 2. Adopting the idea of Zhang et al. [7], the local contact angle $\theta_i(\boldsymbol{x})$ at coordinates $\boldsymbol{x}$ of phase i is determined based on the phase fractions f_j and f_k via

$$\theta_i(\boldsymbol{x}) = \frac{f_j(\boldsymbol{x})}{f_j(\boldsymbol{x}) + f_k(\boldsymbol{x})}\theta_{ij} + \frac{f_k(\boldsymbol{x})}{f_j(\boldsymbol{x}) + f_k(\boldsymbol{x})}\theta_{ik}. \tag{4}$$

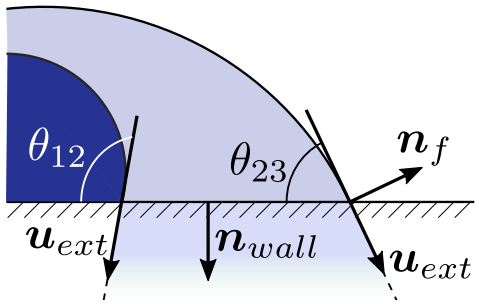

Figure 1. Sketch of Sussman's method. The extension velocity $\boldsymbol{u}_{ext}$ is constructed to transport the liquid according to the contact angle into the ghost cells.

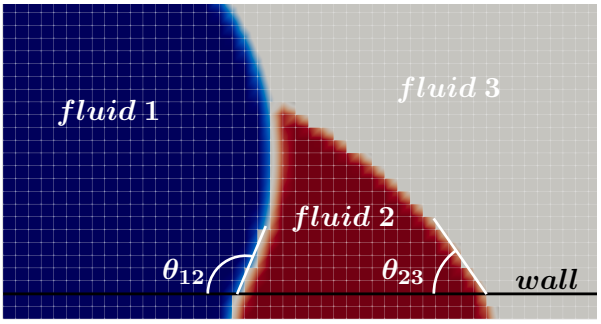

Figure 2. An exemplary VoF distribution after applying Sussman's method. The ghost cells inside the wall boundary contain the information of the extended interfaces.

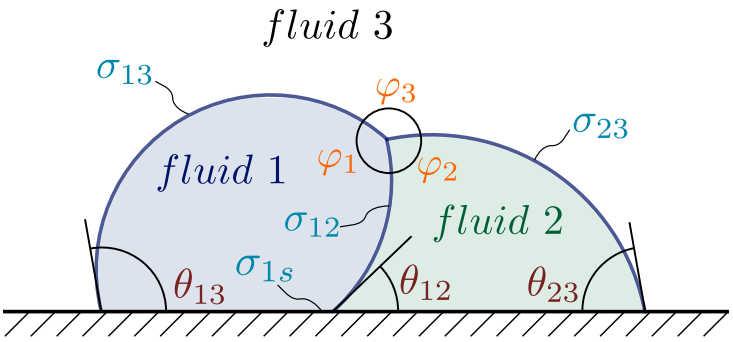

Figure 3. Janus drop configuration with all relevant properties like interfacial tensions σ_{ij}, contact angles θ_{ij}, and interfacial angles φ_i.

This contact angle is then used for the velocity construction in equation 1. In a first step, this procedure is only applied to fluid 1 while neglecting fluid 2 during the advection. Subsequently, the same is carried out for fluid 2. For the final result, the VoF distributions in the ghost cells of both fluids are superimposed. An exemplary VoF distribution is depicted in Figure 2.

Sessile Compound Droplet

Two immiscible liquids with a common interface and in contact with a wall can exhibit four different configurations. The most generic one is the Janus configuration, depicted in Figure 3. Two droplets of immiscible liquids are side by side and in touch with each other and the solid boundary. In total, three distinct contact lines and contact angles where three phases meet are present including the solid phase. Additionally, there are two points where all contact lines meet and hence all four phases exist, cf. Figure 5. The region where all three fluid phases meet is called the triple line and the angles between the three interfaces are the interfacial angles. Each phase has its own properties and characteristics towards other phases. So there are three interfacial tensions σ_{ij}, three solid-fluid interfacial tensions σ_{is}, three contact angles θ_{ij}, and three interfacial angles φ_i. The contact angles as well as interfacial angles obey the conditions

$$\theta_{ij} + \theta_{ji} = \pi, \tag{5}$$

$$\varphi_1 + \varphi_2 + \varphi_3 = 2\pi. \tag{6}$$

For each contact line, Young's equation can be formulated as

$$\sigma_{ij}\cos(\theta_{ij}) = \sigma_{js} - \sigma_{is}. \tag{7}$$

Furthermore, combining equation (7) for all contact angles, the unknown liquid-liquid contact angle can be determined with

$$\theta_{12} = \arccos\left(\frac{\sigma_{13}\cos(\theta_{13}) - \sigma_{23}\cos(\theta_{23})}{\sigma_{12}}\right), \tag{8}$$

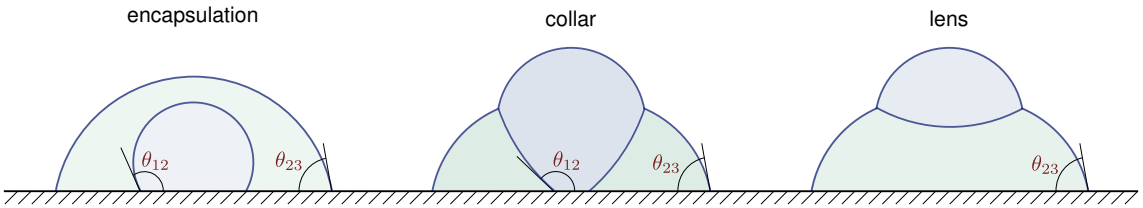

Figure 4. Sketches of the encapsulation, collar, and lens configurations with illustrated contact angles.

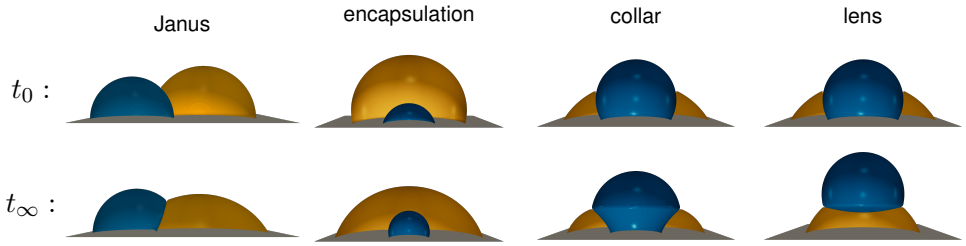

Figure 5. Simulation snapshots of the initial (t_0) and final (t_∞) states for all types of configurations.

as usually the liquid-gas contact angles as well as interfacial tensions can be looked up and in contrast the liquid-liquid contact angle is often unknown or cumbersome to obtain. Other configurations are the encapsulation, collar, and lens configuration, shown in Figure 4. A requirement for the triple line is the inequality

$$\sigma_{ij} < \sigma_{ik} + \sigma_{jk} \tag{9}$$

for all combinations. Otherwise, the liquid with the lower surface tension would cover the other liquid phase to form the encapsulation configuration, so that the surface energy is minimized.

Results and Discussion

The implementation is tested by reproducing all four static configurations of a sessile compound drop. Two immiscible drops are initialized as sections of spheres on a solid substrate in a configuration close to equilibrium. During the simulation, the drops should evolve towards the equilibrium with the correct contact angle. All fluid-fluid interfacial tensions are chosen as $\sigma_{ij} = 30\,\mathrm{mN\,m^{-1}}$ such that all configurations are stable. Solid-fluid interfacial tensions do not need to be specified explicitly but are fixed implicitly by assigning the contact angles. Moreover, the liquid-gas contact angles are set to $\theta_{13} = 90°, \theta_{23} = 70°$ which yields a liquid-liquid contact angle of $\theta_{12} = 110°$. Figure 5 displays snapshots of the initial (t_0) and final (t_∞) state of four different simulations. All types of configurations are reproduced by the simulation and the droplets seem to adopt the correct contact angles. Interestingly, the initial setup for the collar and lens shapes is the same. Only the dynamic viscosity differs by a factor of 10 as $\mu_{collar} = 10\mu_{lens}$. This demonstrates that there is not always one unique stable solution and the dynamics can have an impact on the final state.

Conclusion

The solver FS3D was extended for simulations of wetting phenomena of a ternary system in contact with a wall. The implementation was tested to reproduce four different types of configurations that a sessile compound drop can exhibit. We therefore conclude that the presented framework is able to predict wetting phenomena of a ternary system. In future work, the simulation of dynamic contact lines will be pursued further to enable the simulation of compound droplet impacts with multiple contact lines.

Acknowledgment

We kindly acknowledge funding by the Deutsche Forschungsgemeinschaft (DFG) under Project-ID 270852890 – GRK 2160/2 and under Germany's Excellence Strategy – EXC 2075 – 390740016.

Nomenclature

f	phase fraction [-]	Δz	grid spacing [m]
$\boldsymbol{n}$	normal vector [-]	θ	contact angle [°]
$\boldsymbol{u}_{ext}$	extension velocity [m/s]	μ	dynamic viscosity [Pa s]
$\boldsymbol{x}$	coordinates [m]	σ	surface tension [N/m]
Δt	time step [s]	φ	interfacial angle [°]

References

[1] R. G. Cox. The dynamics of the spreading of liquids on a solid surface. part 1. viscous flow. *Journal of Fluid Mechanics*, 168(1):169, 1986.

[2] K. Eisenschmidt, M. Ertl, H. Gomaa, C. Kieffer-Roth, C. Meister, P. Rauschenberger, M. Reitzle, K. Schlottke, and B. Weigand. Direct numerical simulations for multiphase flows: An overview of the multiphase code FS3D. *Journal of Applied Mathematics and Computation*, 272(2):508–517, 2016.

[3] C. W. Hirt and B. D. Nichols. Volume of fluid (VOF) method for the dynamics of free boundaries. *Journal of Computational Physics*, 39(1):201–225, Jan. 1981.

[4] J. Potyka and K. Schulte. A volume of fluid method for three dimensional direct numerical simulations of immiscible droplet collisions. *International Journal of Multiphase Flow*, 170:104654, 2024.

[5] W. J. Rider and D. B. Kothe. Reconstructing volume tracking. *Journal of Computational Physics*, 141(2):112–152, Apr. 1998.

[6] M. Sussman. *An adaptive mesh algorithm for free surface flows in general geometries*. Chapman and Hall/CRC Boca Raton, FL, USA, 2001.

[7] C.-Y. Zhang, H. Ding, P. Gao, and Y.-L. Wu. Diffuse interface simulation of ternary fluids in contact with solid. *Journal of Computational Physics*, 309:37–51, 2016.

Development of a neural network for determining the behavior of two-phase fluids: the case of sprays and drops

A. Amoresano*, M.Dedes, V.Nebbioso
University of Napoli Federico II, Italy
*Corresponding author: amedeo.amoresano@unina.it

Abstract
The use of high-frequency cameras is a fundamental tool in the study of two-phase fluids such as sprays and droplet behaviour. This paper presents the development of a neural network based on different interpolation criteria to classify images, extract contours and define geometric features in the presence of noise.

Impact of Sparkling Water Droplet: preliminary investigation

L. Araneo*[1], S. Musmeci[1,2], M. Marengo[2]
[1]Politecnico di Milano, Italy
[2]University of Pavia, Italy
*Corresponding author: lucio.araneo@polimi.it

Abstract
The use of high-frequency cameras is a fundamental tool in the study of two-phase fluids such as sprays and droplet behaviour. This paper presents the development of a neural network based on different interpolation criteria to classify images, extract contours and define geometric features in the presence of noise.

Introduction
The dynamic of droplets impacting on dry or wet surfaces is of great importance in many scientific fields and technological applications. The effect of many different parameters have been studied in a variety of studies, including droplet size and velocity, fluid composition and properties, surface material and geometry. In the present work the droplet used are composed either of pure distilled water, or of water with CO2 dissolved in it, to compare the outcome of their impact on two different surfaces.

Method
Distilled water at 10°C, either pure or saturated with CO2 at 3bar, is used to produce droplets of about 3 mm by a syringe pump; the droplets fall on a horizontal surface laying downwards by 5 to 120 cm. The surface can be made of copper or ultrafine sandpaper, either dry or wetted by one previous droplet. Video images are recorded at 200 Hz and analysed to classify the impact outcome. Each test condition is repeated 10 or 20 times for statistical analysis.

Experimental Results
Impact parameter are classified for pure/sparking water, surface type, impact distance, first or second drop (dry/wet).
Impact outcomes are reported in the following tables, where the statistical results are highlighted by a coloured background whose intensity is proportional to each outcome probability.
When impacting on the copper flat surface, differences are negligible (results are not presented). When impacting on the ultrafine sandpaper (P10000), differences appears mostly in the recession after impact, that is present for pure water, while sparking droplets do not recede after their impact and remain pinned to the surface to their larger spreading.

Acqua Demineralizzata, P10000

Quote[m]	N	Deposition	Spreading	Spreading +Receding	Spreading +Receding + Break Up	Prompt Splash	Prompt Splash +Receding	Prompt Splash + RBU	Corona	Corona +Receding	Corona +RBU	Corona splash	Corona splash +Receding	Corona Splash +RBU
0.05	10													
Goccia 1		100%	0%	0%	0%	0%	0%	0%	0%	0%	0%	0%	0%	0%
Goccia 2		100%	0%	0%	0%	0%	0%	0%	0%	0%	0%	0%	0%	0%
0.075														
Goccia 1														
Goccia 2														
0.1	20													
Goccia 1		0%	0%	100%	0%	0%	0%	0%	0%	0%	0%	0%	0%	0%
Goccia 2		0%	0%	0%	0%	0%	0%	0%	0%	10%	45%	0%	10%	35%
0.15	20													
Goccia 1		0%	0%	100%	0%	0%	0%	0%	0%	0%	0%	0%	0%	0%
Goccia 2		0%	0%	0%	0%	0%	0%	0%	0%	0%	0%	0%	30%	70%
0.2	20													
Goccia 1		0%	0%	15%	0%	0%	85%	0%	0%	0%	0%	0%	0%	0%
Goccia 2		0%	0%	0%	0%	0%	0%	0%	0%	0%	0%	0%	30%	70%
0.3	20													
Goccia 1		0%	0%	0%	0%	0%	100%	0%	0%	0%	0%	0%	0%	0%
Goccia 2		0%	0%	0%	0%	0%	0%	0%	0%	0%	0%	0%	75%	25%
0.4	20													
Goccia 1		0%	0%	0%	0%	0%	100%	0%	0%	0%	0%	0%	0%	0%
Goccia 2		0%	0%	0%	0%	0%	0%	0%	0%	0%	0%	0%	100%	0%

Acqua Gasata, P10000													
Quote[m]	N	Deposition	Spreading	Spreading +Receding	Spreading +Receding + Break Up	Prompt Splash	Prompt Splash +Receding	Prompt Splash + RBU	Corona	Corona +Receding	Corona +RBU	Corona splash	Corona splash +Receding	Corona Splash +RBU
0.05	10													
Goccia 1		100%	0%	0%	0%	0%	0%	0%	0%	0%	0%	0%	0%	0%
Goccia 2		100%	0%	0%	0%	0%	0%	0%	0%	0%	0%	0%	0%	0%
0.075														
Goccia 1														
Goccia 2														
0.1	10													
Goccia 1		0%	100%	0%	0%	0%	0%	0%	0%	0%	0%	0%	0%	0%
Goccia 2		0%	0%	0%	0%	0%	0%	0%	40%	0%	0%	60%	0%	0%
0.15	10													
Goccia 1		0%	60%	0%	0%	40%	0%	0%	0%	0%	0%	0%	0%	0%
Goccia 2		0%	0%	0%	0%	0%	0%	0%	0%	0%	0%	100%	0%	0%
0.2	10													
Goccia 1		0%	0%	0%	0%	100%	0%	0%	0%	0%	0%	0%	0%	0%
Goccia 2		0%	0%	0%	0%	0%	0%	0%	0%	0%	0%	100%	0%	0%
0.3														
Goccia 1														
Goccia 2														
0.4	10													
Goccia 1		0%	0%	0%	0%	100%	0%	0%	0%	0%	0%	0%	0%	0%
Goccia 2		0%	0%	0%	0%	0%	0%	0%	0%	0%	0%	100%	0%	0%

Conclusion

It is evident that the dissolved CO2 influences the droplet impact outcome in some specific conditions, while in other conditions its presence has no evident effect. These results forster for further study on sparkling droplet impact.

Analytical Prediction of Transient Spray Cooling

N. Banerjee[1], M. Marengo[1] and C. Tropea[2]
[1]University of Pavia, Italy
[2]Technical University Darmstadt, Germany
*Corresponding author: marco.marengo@unipv.it

Abstract

Spray cooling is a well-established technique for high-flux thermal management in applications ranging from metal quenching and turbine blade protection to the cooling of compact, high-power electronics [6, 5, 3]. A critical challenge in optimizing spray cooling lies in accurately modeling the transient thermal response of the substrate, especially as it passes through different boiling regimes: film boiling, transitional boiling, and nucleate boiling. This study presents a physics-informed, computationally efficient framework to simulate such transient spray cooling under a single nozzle, offering predictive insights that complement experimental investigations.

The model is grounded in analytical expressions that describe the heat transfer from individual droplet impacts in each boiling regime. These expressions are sourced from validated literature and incorporate regime-specific physical mechanisms. The transition between boiling regimes is governed by temperature-based thresholds, allowing the simulation to dynamically adapt as the substrate cools. By applying the principle of superposition, the model aggregates the contribution from all impacting droplets based on their spatial and temporal number flux to calculate the instantaneous heat removal rate from the surface.

A full conjugate heat transfer problem is solved using a finite difference approach, enabling time-resolved prediction of the temperature distribution within the substrate [1].

This modeling framework is further extended to evaluate the performance of Intermittent Spray Cooling (ISC), where cooling is applied in bursts rather than continuously [4]. ISC is characterized by two key parameters: duty cycle (ϕ) and cycle frequency (f).

The study demonstrates that by adjusting these parameters—particularly increasing the spray-on phase duration (ton)—ISC can achieve faster and more efficient cooling than continuous spray cooling, especially in the film boiling regime where droplet-induced vapour disruption is most beneficial.

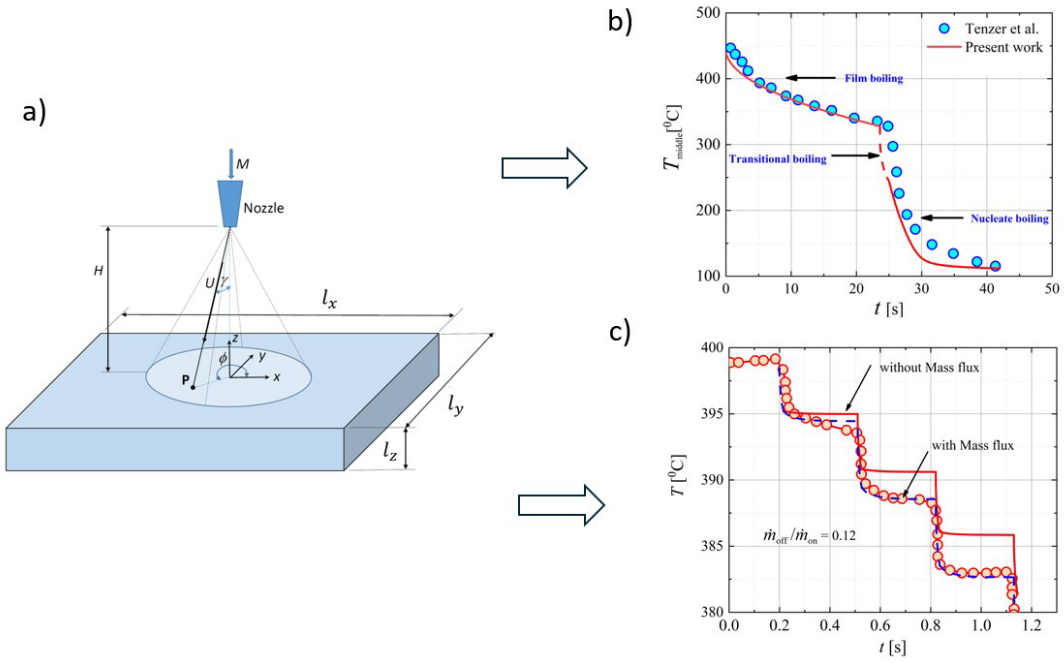

Figure 1. a) Sketch of the geometric parameters defining the geometry of the substrate and spray cooling. b) Validation of transient behaviour of temperature at the center of the heated surface performed in [7] using the parameters D0 = 50 µm, U0 =13 m/s, Tw0 = 450◦C and mass flow rate ˙M = 0.1 kg/s. c) Comparison of experiment performed in [2] with predictions. Substrate surface temperature is shown as a function of time. Cycle time of the intermittent spray is 300 ms and duty cycle is φ = 0.05. Solid red line is with zero mass flux during Toff period. Dashed blue line corresponds to a mass flux of 12% of the ton mass flux during the toff period. Input conditions are: ˙M = 0.5 kg/m2s, U0 = 5 m/s, D0 = 50 µm, H = 0.15 m, and γmax = 12.5 ◦.

Model validation is performed using published experimental data [7, 2], confirming its ability to capture the thermal response of the substrate with high fidelity. A comprehensive parametric analysis is then conducted to examine the influence of spray characteristics—including droplet size, velocity, and flux—on the substrate cooling behavior. The results reveal that ISC offers not only energy and fluid savings but also improved control over surface temperature trajectories, making it particularly attractive for applications requiring precision thermal management.
Overall, this study contributes a versatile, physics-based modeling tool for engineers and researchers, providing deep insights into spray cooling dynamics across all boiling regimes.
The framework offers a valuable foundation for optimizing ISC strategies and guiding future experimental and industrial developments in advanced cooling technologies.

Keywords: intermittent spray cooling, duty cycle, film boiling, frequency.

References

[1] Banerjee, N., Tropea, C., Seshadri, S., 2025. Transient spray cooling: An analytic predictive approach. Physical Review Fluids 10, 053602.
[2] Fest, S., Schmidt, J., 2008. Intermittent spray cooling of metals at surface temperatures above the Leidenfrost point, in: 22nd European Conference on Liquid Atomization and Spray Systems, 7th-10th September.
[3] Mascarenhas, N., Mudawar, I., 2010. Analytical and computational methodology for modeling spray quenching of solid alloy cylinders. International Journal of Heat and Mass Transfer 53, 5871–5883.
[4] Pan˜ao, M., Moreira, A., 2005. Thermo-and fluid dynamics characterization of spray cooling with pulsed sprays. Experimental Thermal and Fluid Science 30, 79–96.
[5] Price, R., Fletcher, A., 1980. Determination of surface heat-transfer coefficients during quenching of steel plates. Metals Technology 7, 203–211.
[6] Santofimia, M., Zhao, L., Sietsma, J., 2011. Overview of mechanisms involved during the quenching and partitioning process in steels. Metallurgical and Materials Transactions A 42, 3620–3626.
[7] Tenzer, F.M., Roisman, I.V., Tropea, C., 2019. Fast transient spray cooling of a hot thick target. Journal of Fluid Mechanics 881, 84–103.

A HHO formulation for variable density incompressible flows where the density is purely advected

L.A. Botti*, F.C. Massa
Università degli Studi di Bergamo; Viale Marconi 5, 24044 Dalmine, BG, Italy
*Corresponding author: lorenzo.botti@unibg.it

Abstract
We propose a Hybrid High-Order formulation for variable density incompressible flows where all unknowns are hybridized. Accordingly, velocity, pressure and density are discretized based on polynomial functions whose support is both the mesh and the mesh skeleton.
The model is based on conservation of volume, conservation of mass and balance of linear momentum. Since, by construction, the velocity field is pointwise divergence-free and the normal trace of the velocity is continuous on inter-element boundaries, conservation of volume is exactly satisfied at the discrete level. As a result, mass conservation states that density is a purely advected quantity. The formulation is pressure-robust, meaning that irrotational body forces only affect the pressure field and the velocity error is insensitive to the pressure error.
Time integration is carried out based on fully implicit ESDIRK schemes and efficiency of the solution strategy is achieved relying on static condensation and multilevel preconditioners.
To validate the implementation, we consider test cases where initial and boundary conditions are imposed according to manufactured solutions and we evaluate the spatial and temporal convergence rates. In order to highlight the benefits of the formulation in practice, several flow problems of benchmark will be performed.

Measurement of interfacial stress from interface curvature

P. Di Marco and A.I. Garivalis
University of Pisa, Italy
*Corresponding author: p.dimarco@ing.unipi.it

Abstract

The momentum balance of an interface subjected to superficial stresses and of curvature K, if projected in the direction normal to the interface $\mathbf{n}_A$, leads to the capillary equation

$$(\dot{m}'_A \vec{v}_A \cdot \mathbf{n}_A - \dot{m}'_B \vec{v}_B \cdot \mathbf{n}_B) + p_B - p_A + \mathbf{n}_A \cdot \left(\underline{\underline{\mathbf{T}}}_{e,A} - \underline{\underline{\mathbf{T}}}_{e,B} \right) \cdot \mathbf{n}_A + \mathbf{n}_A \cdot \left(\underline{\underline{\mathbf{T}}}_{v,A} - \underline{\underline{\mathbf{T}}}_{v,B} \right) \cdot \mathbf{n}_A = 2\sigma K$$

where the first term is the so-called recoil force (due to momentum flux on both sides of interface), σ is the surface tension, K is the interface curvature, p_A and p_B are the pressures on the two sides of the interface. The deviatoric viscous tensor and the electric stress tensors, $\mathbf{T}_v$, $\mathbf{T}_e$, are finally included.

Generally, this equation is considered in its static version, leading to the celebrated Laplace-Young equation

$$p_A - p_B = 2\sigma K$$

which states that the pressure is always greater on the concave side of the interface, regardless of which fluid (liquid or vapour) occupies that side. So the equation can be equally applied to bubbles and drops.

Later on, Lord Rayleigh extended the equation including the dynamic pressure due to the motion of the fluid on both sides of interface, and Plesset included viscous forces. In recent times, electric stress was added too.

The aim of this work is to illustrate some case studies where, once the curvature is experimentally measured by means of image processing and the hydrostatic pressure is known, the remaining forces, if present, can be determined by equilibrium unbalance and compared with theoretical models.

A structure preserving discretization of a unified HTC multiphase model of continuum mechanics

L D. Ferrari*, I. Peshkov, E. Romenski and M. Dumbser
[1]Laboratory of Applied Mathematics, DICAM, University of Trento, Italy
*Corresponding author: davide.ferrari@unitn.it

Abstract
I will present a new structure preserving scheme to mimic at the discrete level some mathematical properties of the multiphase diffuse-interface model that we have recently formulated in the framework of Thermodynamically Compatible Hyperbolic equations, see [1]. The thermodynamic compatibility at the discrete level is achieved through the numerical flux correction recently introduced by Abgrall et al. The consistency with the second law of thermodynamics is satisfied through an appropriate thermodynamically compatible parabolic vanishing viscosity regularization, as well as through an opportune discretization of dissipative processes defined on a continuous level. Moreover, space will be devoted to the derivation of an appropriate discretization that preserves certain nonlinear algebraic constraints of the system of equations, in particular those relating to the physical bounds on density and volume fraction. To this end, a more classical but equivalent form of the PDEs system will be considered, which favours the time evolution of non-dimensional quantities, such as volume fractions. A simple positivity condition can be derived for the numerical solution of these specific non-conservative volume fraction evolution equations.
Then, at the discrete level, an appropriate discretization is achieved, which allows discrete equivalence between the two forms of the PDE system. The validation process includes a wide range of benchmarks and several applications to compressible multiphase problems.

References
[1] D. Ferrari and I. Peshkov and E. Romenski and M. Dumbser, A unified SHTC multiphase model of continuum mechanics, arXiv preprint, arXiv:2403.19298, 2024.

Transcritical sprays: Towards drop sizing by polarized Mie scattering with structured illumination

G. Lamanna*, V. Mrotzek, C. Steinhausen
University of Stuttgart, Germany
*Corresponding author: grazia.lamanna@itlr.uni-stuttgart.de

Abstract
This work describes the application of planar structured laser illumination to near-critical jets. The latter exhibit a complex interplay between compressible fluid dynamics and non-equilibrium phase transitions, which occur on a very small temporal and spatial scale. These features pose several constraints on the application of structured laser illumination. In this work, we present our optical design, aimed at enabling droplet sizing by polarised Mie.

An Experimental Setup for Impingement of Liquid Gallium

A. Lankry[1], Y. Amsalem[1], M. Vaknin[1], M. Arogeti[2], T. Bar-Kohany[1]
[1]Mechanical Engineering, NRCN, Beer Sheva, Israel.
[2]Mechanical Engineering, Sami Shamoon College of Engineering, Beer Sheva, Israel
*Corresponding author: talibk@tauex.tau.ac.il

Abstract
High-quality sprays with well-defined characteristics are essential for various industrial applications.
Understanding the dynamics that follow a droplet's impact on a solid surface is crucial for controlling liquid flow in processes ranging from aerosol and spray generation to drop-on-demand printing. The performance and quality of these systems depend significantly on design considerations.
Liquid metal sprays are particularly valuable for applications such as coating and surface treatments [1]. Among the elements in the periodic table, only mercury is a metallic liquid at room temperature. Four additional metals — francium, cesium, gallium, and rubidium—are liquids just above room temperature. The liquid state of these metals arises from the weak binding of their electrons to the atomic nucleus, which limits electron sharing between atoms and facilitates their transition from solid to liquid.
This study builds upon previous research [2]-[4] to investigate the spreading dynamics of liquid gallium, a metal of growing interest due to its unique properties. To enable these experiments, a specialized system was designed and constructed. The setup features a glovebox filled with heated inert argon gas, maintaining an oxygen-free environment, and includes a heating mechanism to raise the gallium to the desired temperature.
The system is equipped with high-speed imaging capabilities to capture and analyze the spreading behavior of gallium droplets in detail. This experimental approach aims to advance the understanding of liquid metal dynamics and inform the development of improved spray systems for industrial use.

Keywords: Drop impact, Liquid gallium, Deposition, Experimental study, Impingements

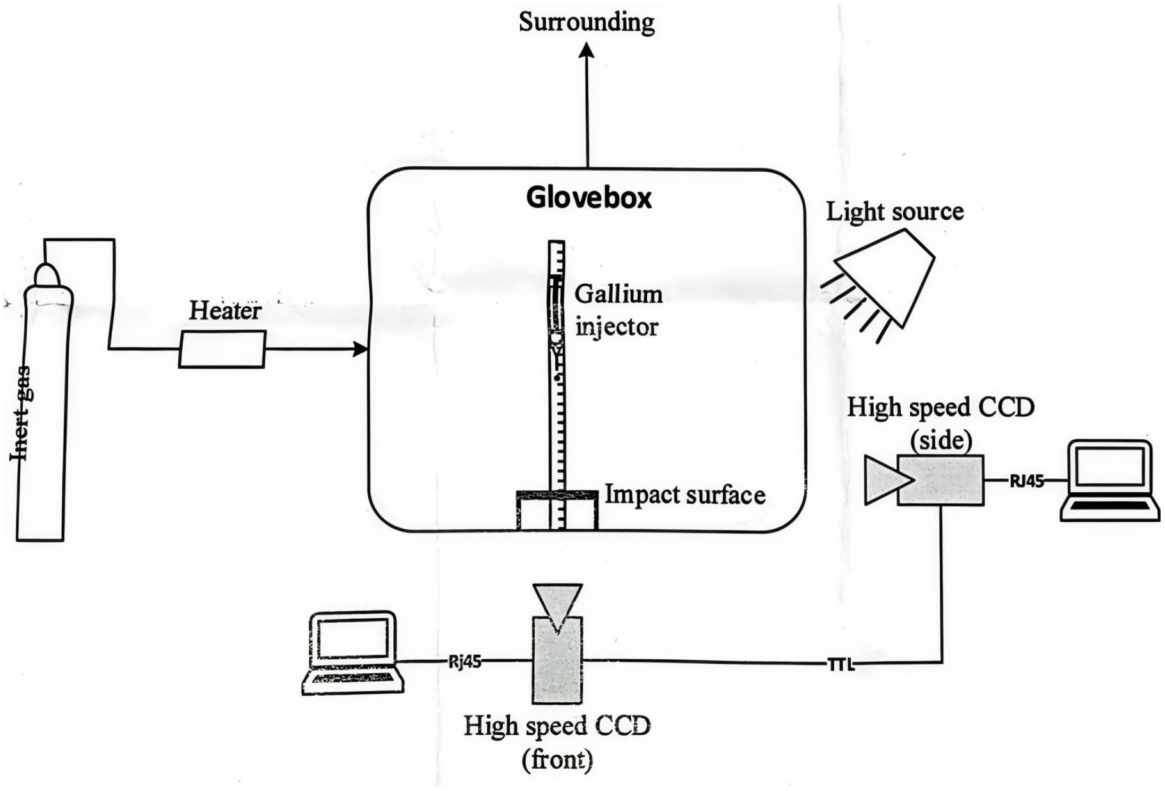

Figure 1. Graphical description of the experimental setup.

Recent advances in droplet modelling using the Full Lagrangian Approach

C. Stafford[1], Z. Nissar[2], G. de Sercey[2], S. Begg[2], O.Rybdylova*[2]
[1]Department of Chemical and Biological Engineering, Iowa State University, USA
[2]Advanced Engineering Centre, School of Architecture, Technology and Engineering, University of Brighton, UK
*Corresponding author: O.Rybdylova@brighton.ac.uk

Abstract
Sprays are wide-spread in daily life, examples include aerosols generated when coughing, sprays used for cooling or surface coating. The Full Lagrangian Approach (FLA) is known for its advantages in application to particle-laden flows. This approach makes it possible to capture detailed structures in the particulate clouds, including where particle trajectories cross and particles collect in narrow regions. It has proven to be an efficient approach for dilute mixtures and recently it was applied to polydisperse evaporating sprays. In this presentation, we will present the recent development of the FLA, including a generalised FLA and experimental work designed for the FLA validation.

Author index